Kinetochore Microtubules indirectly link Chromosomes and Centrosomes in *C. elegans* Mitosis

Stefanie Redemann[1*], Johannes Baumgart[2*], Norbert Lindow[3], Sebastian Fürthauer[4], Ehssan Nazockdast[4], Andrea Kratz[3], Steffen Prohaska[3], Jan Brugués[2,5,6], Michael Shelley[4], and Thomas Müller-Reichert[1]

[1]Experimental Centre, Medical Faculty Carl Gustav Carus, Technische Universität Dresden, 01307 Dresden, Germany
[2]Max Planck Institute for the Physics of Complex Systems, 01187 Dresden, Germany
[3]Zuse Institute Berlin, 14195 Berlin, Germany
[4]The Courant Institute of Mathematical Sciences, New York University, New York, NY 10012, USA, and Centre for Computational Biology, The Simons Foundation, New York, NY 10011
[5]Max Planck Institute of Molecular Cell Biology and Genetics, 01307 Dresden, Germany
[6]Centre for Systems Biology Dresden, 01307 Dresden, Germany
[*]joint first authors

Key words: microtubules, kinetochore microtubules, mitosis, spindle, centrosomes, kinetochores, chromosome segregation, electron tomography, 3D reconstruction, EBP-2 tracking, FRAP, stochastic simulation of microtubule dynamics

Abstract:

The mitotic spindle is a dynamic microtubule-based apparatus that ensures the faithful segregation of chromosomes by connecting chromosomes to spindle poles. How this pivotal connection is established and maintained during mitosis is currently debated. Here we combined large-scale serial electron tomography with live-cell imaging to uncover the spatial and dynamic organization of microtubules in the mitotic spindles in *C. elegans*. With this we quantified the position of microtubule minus and plus-ends as well as distinguished the different classes of microtubules, such as kinetochore, astral and spindle microtubules with their distinct properties. Although microtubules are nucleated from the centrosomes, we find only a few, if any, kinetochore microtubules directly connected to the spindle poles, suggesting an indirect pole to chromosome connection. We propose a model of kinetochore microtubule assembly and disassembly, in which microtubules undergo minus-end depolymerisation, resulting in a detachment from the centrosome. Our reconstructions and analyses of complete spindles expand our understanding of spindle architecture beyond the light microscopic limit.

Introduction

The mitotic spindle is a dynamic microtubule-based apparatus that ensures the segregation of chromosomes during cell division. Its properties are governed by an array of factors, such as polymerases, depolymerases, motor proteins, cross-linkers and other microtubule associated proteins [1]. Remarkably, despite the high turnover of microtubules the spindle maintains its integrity throughout mitosis. In particular it is crucial that the mechanical connection between chromosomes and the spindle poles is maintained, since it allows chromosomes to be transported to the cell poles during division. How kinetochore microtubules (KMTs) connect to chromosomes varies between organisms. In mammals, microtubules attach to monocentric kinetochores that are located at specific sites on the chromosome, whereas nematodes have holocentric kinetochores, for which microtubule-binding sites have no single location on the chromosome. In systems like budding yeast single continuous microtubules span the spindle pole-to-chromosome distance [2], whereas in mammalian systems, kinetochores and centrosomes are directly connected by bundles of microtubules, called kinetochore fibres. Other systems do not have direct connections at all. In *Xenopus* extract spindles, the link seems to be established by multiple connections between shorter microtubules [3].

Most of the information we currently have about the arrangement and dynamics of microtubules, inferred from light microscopy [3-6], cannot distinguish the different

microtubule subclasses composing the spindle. Electron microscopy has delivered invaluable data on cellular organization, but there is surprisingly little quantitative data on the fine structure of mitotic spindles, and is mostly limited to *S. cerevisiae* [2], partial reconstructions of PTK2 cells in culture [7], and early *C. elegans* embryos [8, 9]. Here, we provide the first full reconstructions of *C. elegans* spindles using electron microscopy. We assess the position and structure of all spindle microtubules, including KMTs, in relation to centrosomes, chromosomes, and each other. Combining this with live-cell imaging allows us to ask questions about spindle architecture, function, and dynamics.

Several proposals have been put forward to explain the origin of KMTs [10-13]. These fall into two major classes. In the first, a radial array of microtubules emanates from centrosomes and those that hit kinetochores bind and become stabilized as KMTs [14, 15]. In the second class, microtubules are instead nucleated around chromosomes and only later attached to kinetochores, as observed in *Xenopus* cell-free extracts [16]. In general, the picture on the origins of KMTs remains fuzzy. While there is additional evidence in *Xenopus* and in mammalian PTK2 cells [4, 17] that microtubules can grow directly from kinetochores, there are also contradictory results on the polarity of the same KMTs from budding yeast [18]. Finally, centrosome and chromosome-based microtubule nucleation are not mutually exclusive and can function together during spindle assembly [19, 20]. Also, an additional mechanism of microtubule nucleation in the bulk of the spindle has been reported [21, 22]. The precise mechanism of KMT formation, however, remains to be determined. It is the aim of the present paper to use

ultrastructural data from electron tomography and live-cell imaging to disentangle which of the proposed mechanism is at work in *C. elegans*, one of the most established model systems in cell biology.

To achieve this, we analysed the number, length distribution, density and dynamics of microtubules in embryonic mitotic spindles of *C. elegans*. Our data suggests that KMTs in *C. elegans* are nucleated around the centrosome. Despite their centrosomal origin, KMTs rarely, if ever, span the entire pole-to-chromosome distance. Based on our analysis we propose that KMTs detach from the centrosomes by depolymerisation from their minus-end. Analysis of microtubule-microtubule interactions further suggests the existence of an indirect centrosome-to-chromosome link.

Results

We quantitatively analysed the 3D organization of mitotic spindles in the single-cell *C. elegans* embryo using electron tomography (Extended Data Fig. 1). This approach allowed us to visualize individual microtubules in metaphase and anaphase spindles (Fig. 1, Supplementary Movie 1, Extended Data Fig. 2). We analysed data per half spindles. A half spindle contained 8524 ± 720 microtubules (s.e.m., $n = 5$), without clear differences between metaphase and anaphase. We divided the reconstructed microtubules into three groups: kinetochore microtubules (KMTs), spindle microtubules (SMTs) and astral microtubules (AMTs). All microtubules ending in the ribosome-free zone around the chromosomes were considered as KMTs (Supplementary Movie 2,3) [8]. Non-KMTs that had their centre of mass within a cone with the opening angle of 18.4° towards the chromosomes were classified as SMTs. All others were considered AMTs (see Supplementary Material).

Kinetochore microtubules randomly attach to holocentric chromosomes

We first used our data to investigate the nature of the attachment of KMTs to the chromosomes. To this end, we projected the positions of all attached KMT ends on to the plane perpendicular to the pole-to-pole axis. There were 6 to 50 KMTs attaching to each of the twelve chromosomes per pole-facing side (Fig. 2a). This is surprisingly close to the number of KMTs attaching to the monocentric mammalian kinetochore [23], despite the larger kinetochore region. We found that the number of attached KMTs correlated

positively with the area of the chromosomes (Extended Data Fig. 3A). The average density of KMTs on the metaphase plates of the five half spindles was from 16 to 27 microtubules/μm^2. Within each dataset the KMT density on the chromosomes was nearly constant (Extended Data Fig. 3b), confirming the holocentric nature of the *C. elegans* kinetochores. We next asked whether the typical distance between KMT minus ends on chromosomes was random or followed a pattern that might reveal the existence of specific attachment sites on the chromosomes. We found the radial distribution function of attachment sites to be roughly uniform with a slightly preferred spacing between the centres of two individual KMT ends of about 127 ± 4 nm (s.e.m., $n = 7$ spindle halves; Fig. 2b) by estimating the position of the first prominent peak. This suggests a well defined distance between nearest neighbours of KMT attachment sites on the chromosomes, hinting at the existence of specific structures on the chromosomes to which KMTs can attach.

Kinetochore microtubules are nucleated at centrosomes

We identified approximately 260 KMTs per half spindle in metaphase ($n = 4$; Fig. 1e and f) and 175 KMTs per half spindle in anaphase ($n = 3$; Fig. 1g and h). This characterization of KMTs allowed us to measure the number density of KMTs to SMTs and their ratio along the half spindle axis, which is approximately 5 μm in length (Fig. 2c). The ratio of the number density of KMTs to SMTs decreases monotonically from chromosomes to poles, dropping from 1.5 to zero (Fig. 2d). This suggests that few, if any, KMTs span the full distance from chromosomes to centrosomes.

Next, we analysed the length distribution of the different microtubule classes. The three classes of microtubules displayed their own distinct length distributions. AMTs have an exponential length distribution (Fig. 3a). The length distribution of SMTs is exponential for shorter lengths (up to 2 μm), similar to AMTs, followed by a flatter distribution up to about 5-7 μm (Fig. 3b). Exponential distributions are typical of dynamic instability kinetics [24-26]. Very differently, KMTs show an apparently uniform length distribution, with only a few short microtubules in their population. Importantly, a role for katanin in severing of KMTs during *C. elegans* mitosis can be excluded [27]. In summary, this suggests that a very different process than those for AMTs and SMTs governs the KMT length distribution.

To explore where in the spindle microtubules nucleate, we analysed the position of microtubules according to their length (Fig. 3d). We found that the majority of short microtubules (below 2 μm) in meta- and anaphase were near the centrosomes. This suggests that most nucleation happens near the centrosomes. However, short KMTs are only found near chromosomes, but are not especially prevalent in that population. We thus asked whether KMTs, unlike the majority of microtubules, nucleate at chromosomes. To investigate this, we analysed the formation of KMTs around chromosomes in one-cell embryos in prometaphase (Extended Data Fig. 4a) and two-cell *zyg-1(RNAi)* embryos with monopolar spindles (Extended Data Fig. 4b-d) [28], where it should be directly observable. Firstly, if microtubules were nucleating around

chromatin, one might expect to see KMTs at the outer side of the metaphase plate, which we do not. Secondly, in both conditions we could not detect any short microtubules on or around chromosomes. Hence, we conclude that the chromosomes are not the site of KMT nucleation.

Most kinetochore microtubules ends are not attached to the centrosomes

Our analysis of the KMT to SMT ratio and the microtubule length distributions suggested that most of the KMTs did not span the entire distance between centrosomes and chromosomes. Next, we analysed the distance of KMT and SMT ends from their mother centrioles and found that 46 ± 4 % (s.e.m., $n = 5$ spindle halves) of the centrosome proximal SMT ends were located within a distance of 2 μm from the mother centriole (Fig. 3e). In contrast, only 22 ± 4 % (s.e.m., $n = 5$ spindle halves) of the KMT ends were within a radius of 2 μm from the mother centrioles, and none closer than 1 μm (Fig. 3f). This lends further support to the idea that the KMTs do not make contact with the centrosomes.

If the KMTs are not directly connected to centrosomes, how is the connection between centrosomes and KMTs established and maintained? To investigate this, we next looked at the end-morphologies of KMTs, as a proxy for their dynamic state [29-32]. In our reconstructions we distinguished open and closed microtubule ends. We found that about 98 % of KMT ends at chromosomes in metaphase and 99% in anaphase displayed an open-end conformation (Extended Data Fig. 5a) with flared ends, which is

consistent with earlier findings [8, 9]. Furthermore, 44 % of the pole-facing ends of KMTs in metaphase and 25% in anaphase were open. We also compared the pole-proximal and distal end-morphology of each individual KMT. The majority of the KMTs had two open ends in metaphase and anaphase. Only 31 % of KMTs in metaphase and 11% of the KMTs in anaphase had one open and one closed end (Extended Data Fig. 5b). Since open ends are thought to be indicative of growth or shrinkage, our data suggest that most of the KMTs have two dynamic ends. Since closed ends are most likely newly nucleated minus ends, we analysed the fraction of closed and open pole-facing microtubule ends with respect to the distance from the centrioles. We found that the fraction of closed ends decreased with increasing distance from the pole, which suggests that most nucleation of KMTs as well as SMTs and AMTs occurs in a zone of about 2-3 μm around the centrioles (Extended Data Fig. 5c,d).

Microtubules grow unidirectionally away from centrosomes and show different dynamics inside the spindle

As the polarity of individual microtubules cannot be clearly determined in our tomograms, we turned to light microscopy to infer the direction of microtubule growth within the spindle. We visualized the motion of growing microtubule plus-ends by live-cell imaging of EBP-2, which specifically binds to the polymerising microtubule plus-ends (Fig. 4) [33]. The mitotic spindle is a crowded environment preventing the tracking of individual EBP-2 comets. Therefore we developed a novel method to analyse the EBP-2 velocity within the spindle based on spatial-temporal correlation. We analysed four

different regions: within the spindle, at chromosomes, and within a central (inner astral) and a peripheral (outer astral) region of the centrosome (Fig. 4a, Supplementary Movie 4). The estimated velocity of the comets was 20.5 ± 1.0 μm/min (s.e.m., $n = 8$ half spindles) in the spindle, 29.1 ± 2.1 μm/min (s.e.m., $n = 8$ half spindles) at chromosomes, and 16.3 ± 1.5 μm/min (s.e.m., $n = 8$ half spindles) in the central region around the centrosome (Fig. 4b). In contrast, we estimated a velocity of about 43.6 ± 1.3 μm/min (s.e.m., $n = 8$ half spindles) in the periphery of the centrosome, suggesting different microtubule dynamics inside spindles than outside of spindles. Additionally, we analysed the direction of EBP-2 comets. This showed that most comets move away from the centrosomes and towards the chromosomes (Fig. 4b), indicating that the majority of minus-ends of microtubules in *C. elegans* spindles are located at the centrosomes, whereas plus-ends grow towards the chromosomes. We challenged this finding by performing laser microsurgery to ablate microtubules within the spindle and so measure their polarity by generating new microtubule plus and minus ends [3]. This microsurgery resulted in the formation of a single wave of depolymerisation of the newly created microtubule plus-ends towards the centrosome (Supplementary Movie 5). This indicates that microtubules within the spindle have the same polarity with the minus-ends oriented towards the poles and the plus-ends facing the chromosomes, thus confirming our EBP-2 data. By combining the dynamic data with the ultrastructural data we are able to determine the position of minus-ends as well as plus-ends within the mitotic spindle.

Chromosome-bound KMT ends are relatively static

After having established that SMTs grow from their plus ends towards the chromosomes, we sought to understand the behaviour of KMT plus-ends. For this, we measured the dynamics of microtubules by FRAP (fluorescence recovery after photo-bleaching) experiments. We bleached a small stripe of approximately 2 μm width in an area close to the chromosomes in metaphase (Supplementary Movie 6). We then analysed the recovery and directionality of the photo-bleached area. The recovery rate in metaphase was approximately $t_{1/2} = 22.6$ (20.7, 24.4) s (95 % CI, $n = 8$ spindles; Fig. 4c), in agreement with previously reported data [34]. To infer the dynamics of the KMT plus ends, which are bound to chromosomes, we measured whether the bleach mark moved. Our analysis showed a weak bias of the photo-bleached region for moving towards the chromosomes, although the velocity detected is 2.8 μm/min and thus closes to our detection limit. However, this finding rules out that microtubules are growing through polymerization at or around chromosomes, since this would result in a motion of the photo-bleached region away from the chromosomes at a velocity that is comparable to the microtubule growth velocity. If anything, the small bias in the opposite direction is consistent with a slow microtubule flux within the *C. elegans* spindle (Fig. 4d).

Microtubules in the mitotic spindle are indirectly coupled

Our observation that the majority of KMTs did not reach the centrosome raised the question of how a strong mechanical connection between chromosomes and centrosomes can be achieved during mitosis. One possibility is that a single KMT is

sufficient for chromosome segregation, as shown in budding yeast [2]. However, given the larger number of KMTs in *C. elegans*, we hypothesized that these KMTs may indirectly connect chromosomes to centrosomes and searched for potential locations of microtubule-microtubule interactions. For such a quantitative network analysis we considered the following parameters: the centre-to-centre distance between two microtubules, the angle between microtubules, and the shortest distance between the pole-proximal end of a non-kinetochore microtubule and the centrosome (Fig. 5a). We started with a neighbour density analysis by measuring the centre-to-centre distance between all microtubules at 25 % and 75 % of the half spindle length (Fig. 5b). In comparison to randomly placed microtubules, this analysis revealed an increased frequency of microtubules with a centre-to-centre distance of 55 ± 4 nm at 25 % as well as at 75 % half spindle length (Fig. 5c and d) by estimating the position of the first prominent peak. This value is larger than the microtubule diameter of about 24 nm. If all microtubules would have a distance of 55 nm to the next neighbour, the density would be four times higher than the maximum measured (Fig. 2c). This indicates a weak clustering. We also looked at the specific neighbour density between different classes of microtubules, e.g. SMTs and KMTs, but could not detect any specific interaction patterns. The measured distances between the microtubules are comparable to the size of microtubule-associated proteins or molecular motors [7, 35, 36]. However, another possibility is that microtubule-microtubule connections might be established by cytoplasmic flow and viscous coupling. The locally higher drag forces between

microtubules that are brought-close together could result in a viscously induced mechanical coupling.

We further aimed to analyse the network capabilities of KMTs and SMTs and used the interaction distance and the interaction angle to describe possible microtubule-microtubule interactions. We plotted the fraction of KMTs that are able to connect to the centrosome by multiple interactions. For different interaction angles (5-45°), we plotted the fraction of KMTs reaching the centrosome within a radius of 1.2 μm as a function of increasing interaction distance (Fig. 5e). This analysis showed that the majority of KMTs could reach the centrosome by interacting with SMTs at a 30-50 nm distance, with an interaction angle of 30-45°. By counting the number of interactions that were needed to reach the centrosome, we show that two interactions are typically sufficient to establish a connection to the centrosome in metaphase (Fig. 5f). This implies the formation of a spindle network based on an interaction of KMTs and SMTs, possibly contributing to the integrity of the pole-to-chromosome connection.

Discussion

Combining 3D electron tomography with dynamic light microscopy, we provided quantitative data on mitotic spindles in *C. elegans* with respect to length, end-point position, orientation and interaction of each individual microtubule composing the spindle, and estimated flux and growth velocity within the spindle. This analysis revealed that a few, if any, kinetochore microtubules are directly connected to the spindle poles and suggested an indirect pole-to-chromosome connection. Based on our data, we considered three stochastic models for KMT and SMT dynamics, each illustrated in Fig. 6. In our models SMTs nucleate near the centrosome. We distribute their nucleation positions following the measured distribution of AMT minus-ends within 3 μm of the centriole. From the EBP-2 tracking we have an estimate for the growth velocity of $v_g = 0.4\ \mu$m/s (see Fig. 4b). They undergo catastrophe or reach the chromosomes at which point they become KMTs and no longer undergo catastrophe at their plus ends. The catastrophe rate is estimated from the exponential length distribution of SMT as $\kappa = 0.25\ s^{-1}$ (Fig. 3B). Note that for simplicity, we chose catastrophy from the plus end to immediately destroy the microtubule, and did not track its disassembly process explicitly.

Since KMTs only rarely span the entire chromosome-to-centrosome distance (Figs. 3c, 3f, 5f), we assume that KMTs switch to a shrinking state with a model dependent rate r upon connecting to chromosomes. In the *flux model* (Fig. 6a) we

assume that this switch to shrinking occurs instantaneously ($r \rightarrow \infty$) through an onset of depolymerisation from the attached plus-end, with velocity $v_d = 0.02\ \mu$m/s as suggested by our FRAP measurements (Fig. 4d). The *flux model* can indeed reproduce the observed KMT length distribution (Ext. Fig. 6a). However, it does not reproduce the length distributions of SMTs and the SMT minus end positions, (Ext. Figs. 6b,c). Furthermore, in the *flux model* a *de-novo* generated spindle would take more than 5 minutes to reach its steady state, which is long compared to the typical duration of metaphase in *C. elegans* (Ext. Fig. 6d). We conclude that microtubule plus-end depolymerisation alone is insufficient to explain the data. This suggests that microtubule minus-ends in the spindle are dynamic.

We next asked whether SMTs and KMTs, or only KMTs, can depolymerise from their minus-ends and formulated stochastic models for both scenarios, which we call the *depolymerisation* and *detachment models*, respectively. In the *depolymerisation model* (Fig. 6b) all microtubule minus-ends switch to a shrinking state with a rate r, independent of the state of the plus end. In the *detachment model* (Fig. 6c) only KMTs can switch to a shrinking state. In our simulations, we find that both models can be tuned to reproduce the measured length distribution of KMTs and SMTs (Ext. Figs. 7a,b and 8a,b), while reaching a steady state in under a minute, which is compatible with the duration of mitosis in *C. elegans* (Ext. Figs. 7d and 8d). However, the *detachment model* much better captures the shape of the distribution of KMT length and the SMT minus-end distribution compared to the *depolymerisation model* (Ext. Figs. 7a,c and 8a, c). In

conclusion, these findings suggest that minus-ends of KMTs are selectively destabilized. Plausibly, this could be achieved mechanically through the compressive loads that build on growing KMTs that connect chromosomes to centrosomes or biochemically by post-translational microtubule modifications [37]. Our observation that KMTs link indirectly to spindle poles is in agreement with unattached KMTs in mammalian mitotic spindles [38, 39].

In summary, we have provided precise information on the number, length, density, positions, and dynamics of microtubules in mitotic spindles of the early *C. elegans* embryo. Our approach would be applicable to a number of other model systems, such as *Drosophila, Xenopus,* zebrafish or mammalian cell lines. And, based on our data, large-scale simulations of the choreography of spindle assembly and chromosome segregation could be further developed.

Materials and Methods

Worm strains, gene silencing by RNA interference and feeding clones

C. elegans strains were cultured as described [40]. All strains were maintained at either 16 °C or 25 °C. The following strains were used in this study: wildtype N2 Bristol; MAS37 (unc-119(ed3) III; [pie-1::epb-2-gfp;unc-119(+)] [38, 41]. RNAi experiments were performed by feeding as described [42]. Worms for *zyg-1* (RNAi) were grown for 24 h at 25 °C on feeding plates. A. Hyman (Dresden, Germany) provided the feeding clone for *zyg-1* (F59E12.2).

Sample preparation for electron microscopy

Wild-type N2 *C. elegans* hermaphrodites were dissected in M9 buffer and single embryos early in mitosis were selected and transferred to cellulose capillary tubes (Leica Microsystems, Vienna, Austria) with an inner diameter of 200 µm. The embryos were observed with a stereomicroscope until either metaphase or anaphase and then immediately cryo-immobilized using an EM PACT2 high-pressure freezer equipped with a rapid transfer system (Leica Microsystems, Vienna, Austria) as previously described [43]. Freeze substitution was performed over 3 d at -90 °C in anhydrous acetone containing 1 % OsO_4 and 0.1 % uranyl acetate using an automatic freeze substitution machine (EM AFS, Leica Microsystems, Vienna, Austria). Epon/Araldite infiltrated samples were flat embedded in a thin layer of resin, polymerised for 3 d at 60 °C, and selected by light microscopy for re-mounting on dummy blocks. Serial semi-thick

sections (300 nm) were cut using an Ultracut UCT Microtome (Leica Microsystems, Vienna, Austria). Sections were collected on Formvar-coated copper slot grids and poststained with 2 % uranyl acetate in 70 % methanol followed by Reynold's lead citrate [44].

Electron tomography

Dual-axis electron tomography was performed as described [45]. Briefly, 15 nm colloidal gold particles (Sigma-Aldrich) were attached to both sides of semi-thick sections collected on copper slot grids to serve as fiducial markers for subsequent image alignment. For electron tomography, series of tilted views were recorded using a TECNAI F30 transmission electron microscope (FEI Company, Eindhoven, The Netherlands) operated at 300 kV. Images were captured every 1.0° over a ±60° range and a pixel size of 2.3 nm using a Gatan US1000 CCD camera (2k x 2k). For each serial section two montages of 2 x 3 frames were collected and combined to a supermontage using the IMOD software package to cover the pole-to-pole distance of the spindles [46]. For image processing the tilted views were aligned using the positions of the colloidal gold particles as fiducial markers. Tomograms were computed for each tilt axis using the R-weighted back-projection algorithm [47]. For double-tilt data sets two montages, each consisting of six tomograms, were aligned to each other and combined to a supermontage [45]. In order to cover a large volume of the pole-to-pole region of each mitotic spindle, we recorded on average 24 consecutive serial sections per spindle.

Three-dimensional reconstruction and automatic segmentation of microtubules

We used the IMOD software package (http://bio3d.colourado.edu/imod), which contains all of the programs needed for calculating electron tomograms [46]. Reconstructed tomograms were flattened and the two acquired montages of each section were combined to a supermontage using the *edgepatches, fitpatches* and *tomostitch* commands contained in the IMOD package. We applied the Amira software package for the segmentation and automatic tracing of microtubules [48]. Currently, we use an extension to the filament editor of the Amira visualization and data analysis software [49, 50]. We also used the Amira software to stitch the obtained 3D models in *z* to create full volumes of the recorded spindles [51]. The automatic segmentation of the spindle microtubules was followed by a visual inspection of the traced microtubules within the tomograms and correction of the individual microtubule tracings. Corrections included: manual tracing of undetected microtubules, connection of microtubules and deletions of tracing artifacts (e.g. membranes of vesicles). Approximately 5 % of microtubules needed to be corrected.

Data analysis

Data analysis was performed using either the Amira software or by exporting the geometric data of the traced microtubules followed by an analysis using Matlab (R2015b, The MathWorks Inc., Nitick, USA). The microtubule neighbourhood densities for 2D slices in comparison to random samples and random displacements were

computed in two steps. First, a set of uniformly distributed slices is defined for half of a microtubule spindle from the centrosome to the chromosomes perpendicular to the pole-to-pole axis given by the mother centriole. Additionally, a cone is defined with the same axis and the top at the centre of the mother centriole and an opening angle of 18.4° measured from the axis to the lateral surface. Given, a cone angle, each slice is bound by the intersection circle of the cone with the slice. Then, all intersections of the microtubules inside the circles are determined. In the second step, the radial distribution function is estimated. For each microtubule point, the local density in a range of radial distance is computed. The mean over all microtubules provides an estimate for the radial distribution function as a neighbourhood density. For the normalization we use 10,000 sets of randomly displaced microtubules and for purely randomly placed microtubules with the same total number and no preferred location.

For the detection of possible interactions in 3D, a 3-step algorithm was implemented in Amira. First, for each microtubule, the distance to the centriole was computed and all microtubules with a distance smaller than were marked as connected to the centrosome. It is important to note here that each microtubule is represented as a piece-wise linear curve. For each line segment of a microtubule the distance to the centriole, which is represented as a point, was computed analytically. The distance of a microtubule was defined as the minimum of all segment distances. In the second step, for each pair of microtubules the distance and the angle were computed. The distance between two microtubules was defined as the minimum of the distances between all

their line segments. A 3D grid data structure was used to accelerate these computations. To reduce errors due to local distortions of the microtubules, the angle is defined by the angle between the lines through the start and end points of the microtubules. Based on these pre-computations, in the third step an abstract graph was constructed, where each microtubule is represented as a vertex and each interaction (based on thresholds for interaction distance and angle) as an edge. Finally, for each kinetochore microtubule the shortest path to a microtubule marked as connected to the centrosome was computed in the graph using Dijkstra's algorithm.

Error analysis

For the complete imaging and reconstruction pipeline of a spindle, the following errors need to be investigated. First, during the data preparation and the imaging process, the tomograms are locally distorted. Furthermore, the exposure of the electron beam causes a shrinking of the sample. During the reconstruction of the microtubules, however, most errors occur in the tracing and matching process. Additionally the data is again distorted in all directions to align the tomograms. We assume that this distortion primarily compensates the distortion of the imaging process. For the tracing, the error was previously analysed for reconstructions of *C. elegans* centrosomes [49]. Although the spindle data is larger, the tomogram content is similar to the centrosome data sets, and thus we assume that the error lies in the same range of 5-10 %. In addition, the traced microtubules were manually verified. It is more difficult to estimate the error of the matching algorithm [51], since it depends on the local density and properties of the

microtubules. For this reason, the stitched microtubules were manually verified and corrected for all KMTs. The quality of the analysis of the KMTs, therefore, should be influenced only by minor 3D distortions. In order to estimate the overall quality of the stitching the distribution of MT endpoints in z-direction (i.e. normal to the plane of the slice) was analysed by binning the endpoints in z-direction (Supplementary Fig. 9). Bins were fixed to be either inside a section (50 % in z-direction, centred) or across a boundary between sections (25 % in z-direction of either adjacent section). In order to account for a varying section thickness a MT endpoint density (in z-direction) was defined by normalizing over the width of these bins. We assume that high quality stitching would result in a smooth curve. However we did detect some peaks within the histograms. Generally most of these peaks are found within the sections. This can be explained by the fact that the boundary regions of a tomogram are often blurry and MTs are possibly not traced within this area. This would explain systematically lower endpoint number in boundary regions and the saw tooth features in the histograms. This may be especially relevant in regions were MT run parallel to boundaries.

For the analysis of the microtubules length distributions (Figure 3a,b), we checked whether the microtubules that leave the reconstructed tomographic volume affect our results (approximately 11 μm x 16.5 μm x 6 μm for each half spindle). We removed microtubules with one end point less than 250 nm apart from the boundary of the volume. These microtubules potentially leave the tomographic volume. This had only consequences for the length distribution of the AMTs in terms of the total number

and changed only slightly the shape of the distribution. Furthermore, in all analyses, microtubules shorter than 100 nm were excluded to reduce errors due to the minimal tracing length. In addition, the end point type could not always be decided during inspection. The number of unclear end points lies in the range of 2 % and is uniformly distributed over the kinetochore region. Therefore, we do not expect a relevant error in the analysis.

Light microscopy and Image analysis

Worms were dissected in M9 buffer on a coverslip to obtain embryos. The embryos were then transferred to a glass slide with a 2 % agarose pad. Imaging of the EBP-2::GFP comets was carried out on a Nikon TiE spinning disc confocal microscope using a Nikon Plan-Apochromat 60x water-immersion objective and an iXon EM + DU-897 BV back illuminated EMCCD camera (Andor, Belfast, UK). A single plane was acquired every 250 ms with an exposure of 200 ms starting from metaphase until embryos reached telophase using the IQ3 software (Andor, Belfast, UK). We analysed the local velocities of growing microtubule tips labeled by EBP-2. To obtain a robust estimate in the highly crowded spindle, EBP-2 comets were segmented in each frame using the mosaic suite in Fiji [52]. We then analysed the spatial-temporal correlations of the segmented EBP-2 comets along the radial direction. This approach avoids the problem of identifying the right EBP-2 mark in subsequent frames in a crowded environment. The initial segmentation is necessary as otherwise the signal-to-noise ratio is not sufficient. The spatial-temporal correlations were computed by first resynthesizing movies, where

each identified EBP-2 spot was convolved with a Mexican-hat wavelet. Along the radial direction the size was set to a half pixel size and in the orthogonal direction enlarged by a factor of 4. This ensures that motions along the circumferential direction are still permissible. For the time lag of the spatial-temporal correlations we used 0.6 s and we averaged over all circumferential positions and over the duration of metaphase.

The FRAP experiment was analysed as follows. The position of the two centrosomes was identified and an intensity profile extracted along this axis. We averaged in the perpendicular direction over a distance of 2 μm. The profiles were aligned along the axis by fitting a Gaussian profile to the intensity peak of chromatin, which was labelled by histone::GFP. The photo-bleached region was fitted by a 2nd order polynomial and the location estimated from the position of the minimum. We used the distance between these two to estimate the velocity of the photo-bleached region with respect to the initial position. For the recovery we analysed the amplitude at the centre of the photo-bleached region with respect to the intensity at the mirrored position on the axis.

Stochastic simulations

We performed stochastic simulations for three different models of microtubule dynamics, which we call the *flux model*, the *depolymerisation model*, and the *detachment model*, respectively. The stochastic models were implemented using a standard Gillespie algorithm. In all three models microtubules are nucleated as SMTs

with an initial length of zero near in the vicinity of the centrosome. The exact nucleation position is drawn from the measured distribution of AMT minus ends that are within 3 μm of the centriole. The total rate of nucleation is fixed by requiring for the number of KMTs in steady state to become comparable to measured numbers, i.e. around 250.

In all three models, after nucleating, SMTs grow with a velocity $v_g = 0.4\ \mu$m/s (as measured; see Fig. 4b) from the plus-end, until they either undergo catastrophe with rate $\kappa = 0.25\ s^{-1}$ (as estimated from the decay of the length distribution of short SMTs) resulting in their immediate removal, or they reach the chromosomes which are positioned $L = 6.5\ \mu$m away from the centrosomes (as measured from ultrastructure). SMTs, which reach the chromosomes become KMTs, no longer undergo catastrophe from their plus-ends, and remain attached to the chromosomes. Note that microtubules keep growing at the same rate then SMTs, even while attached until they switch to their shrinking state in a model dependent way.

The three models differ in the following aspects: In the *flux model*, upon becoming KMTs, KMT plus-ends switch deterministically to shrinking at a velocity $v_d = 0.02\mu$m/s. In the *depolymerisation model*, both KMTs and SMTs can switch to depolymerising from their minus ends with a velocity v_d at a rate r. In the *detachment model*, only KMTs can switch to depolymerising from their minus-ends with a velocity v_d at a rate r. While the *flux model* has no adjustable parameters, in the depolymerisation and detachment models the rate r and the velocity v_d are unknown. Requiring the ratio of SMTs to KMTs to match experiments and mimicking the shape of the experimentally

observed KMT length distribution fix both rates. We summarize all parameters in the Table 1. To compare the outputs of our simulations to the experimental data, we run the simulation sufficiently long to reach a steady-state, and then average over a large number of subsequent steady-state configurations, sampled every thirty seconds to obtain an expectation value and standard deviations for the extracted distributions.

References

1. Helmke, K.J., Heald, R. & Wilbur, J.D. Interplay between spindle architecture and function. *Int Rev Cell Mol Biol* **306**, 83-125 (2013).
2. Winey, M. *et al.* Three-dimensional ultrastructural analysis of the Saccharomyces cerevisiae mitotic spindle. *J Cell Biol* **129**, 1601-1615 (1995).
3. Brugues, J., Nuzzo, V., Mazur, E. & Needleman, D.J. Nucleation and transport organize microtubules in metaphase spindles. *Cell* **149**, 554-564 (2012).
4. Tirnauer, J.S., Canman, J.C., Salmon, E.D. & Mitchison, T.J. EB1 targets to kinetochores with attached, polymerizing microtubules. *Mol Biol Cell* **13**, 4308-4316 (2002).
5. Mitchison, T.J. *et al.* Bipolarization and poleward flux correlate during Xenopus extract spindle assembly. *Mol Biol Cell* **15**, 5603-5615 (2004).
6. Needleman, D.J. *et al.* Fast microtubule dynamics in meiotic spindles measured by single molecule imaging: evidence that the spindle environment does not stabilize microtubules. *Mol Biol Cell* **21**, 323-333 (2010).
7. McDonald, K.L., O'Toole, E.T., Mastronarde, D.N. & McIntosh, J.R. Kinetochore microtubules in PTK cells. *J Cell Biol* **118**, 369-383 (1992).
8. O'Toole, E.T. *et al.* Morphologically distinct microtubule ends in the mitotic centrosome of Caenorhabditis elegans. *J Cell Biol* **163**, 451-456 (2003).
9. McIntosh, J.R. *et al.* Conserved and divergent features of kinetochores and spindle microtubule ends from five species. *J Cell Biol* **200**, 459-474 (2013).
10. Hallen, M.A. & Endow, S.A. Anastral spindle assembly: a mathematical model. *Biophys J* **97**, 2191-2201 (2009).
11. Loughlin, R., Heald, R. & Nedelec, F. A computational model predicts Xenopus meiotic spindle organization. *J Cell Biol* **191**, 1239-1249 (2010).
12. Paul, R. *et al.* Computer simulations predict that chromosome movements and rotations accelerate mitotic spindle assembly without compromising accuracy. *Proceedings of the National Academy of Sciences of the United States of America* **106**, 15708-15713 (2009).
13. Brugues, J. & Needleman, D. Physical basis of spindle self-organization. *Proceedings of the National Academy of Sciences of the United States of America* **111**, 18496-18500 (2014).
14. Hayden, J.H., Bowser, S.S. & Rieder, C.L. Kinetochores capture astral microtubules during chromosome attachment to the mitotic spindle: direct visualization in live newt lung cells. *J Cell Biol* **111**, 1039-1045 (1990).
15. Rieder, C.L. & Alexander, S.P. Kinetochores are transported poleward along a single astral microtubule during chromosome attachment to the spindle in newt lung cells. *J Cell Biol* **110**, 81-95 (1990).
16. Heald, R. *et al.* Self-organization of microtubules into bipolar spindles around artificial chromosomes in Xenopus egg extracts. *Nature* **382**, 420-425 (1996).
17. O'Connell, C.B., Loncarek, J., Kalab, P. & Khodjakov, A. Relative contributions of chromatin and kinetochores to mitotic spindle assembly. *J Cell Biol* **187**, 43-51 (2009).
18. Kitamura, E. *et al.* Kinetochores generate microtubules with distal plus ends: their roles and limited lifetime in mitosis. *Dev Cell* **18**, 248-259 (2010).
19. Bonaccorsi, S., Giansanti, M.G. & Gatti, M. Spindle self-organization and cytokinesis during male meiosis in asterless mutants of Drosophila melanogaster. *J Cell Biol* **142**, 751-761 (1998).

20. Khodjakov, A., Cole, R.W., Oakley, B.R. & Rieder, C.L. Centrosome-independent mitotic spindle formation in vertebrates. *Current biology : CB* **10**, 59-67 (2000).
21. Goshima, G., Mayer, M., Zhang, N., Stuurman, N. & Vale, R.D. Augmin: a protein complex required for centrosome-independent microtubule generation within the spindle. *J Cell Biol* **181**, 421-429 (2008).
22. Petry, S., Groen, A.C., Ishihara, K., Mitchison, T.J. & Vale, R.D. Branching microtubule nucleation in Xenopus egg extracts mediated by augmin and TPX2. *Cell* **152**, 768-777 (2013).
23. McEwen, B.F., Hsieh, C.E., Mattheyses, A.L. & Rieder, C.L. A new look at kinetochore structure in vertebrate somatic cells using high-pressure freezing and freeze substitution. *Chromosoma* **107**, 366-375 (1998).
24. Mitchison, T. & Kirschner, M. Dynamic instability of microtubule growth. *Nature* **312**, 237-242 (1984).
25. Mitchison, T. & Kirschner, M. Microtubule assembly nucleated by isolated centrosomes. *Nature* **312**, 232-237 (1984).
26. Dogterom, M. & Leibler, S. Physical aspects of the growth and regulation of microtubule structures. *Phys Rev Lett* **70**, 1347-1350 (1993).
27. Srayko, M., O'Toole E, T., Hyman, A.A. & Muller-Reichert, T. Katanin disrupts the microtubule lattice and increases polymer number in C. elegans meiosis. *Current biology : CB* **16**, 1944-1949 (2006).
28. O'Connell, K.F. *et al.* The C. elegans zyg-1 gene encodes a regulator of centrosome duplication with distinct maternal and paternal roles in the embryo. *Cell* **105**, 547-558 (2001).
29. O'Toole, E., Greenan, G., Lange, K.I., Srayko, M. & Muller-Reichert, T. The Role of gamma-Tubulin in Centrosomal Microtubule Organization. *PloS one* **7**, e29795 (2012).
30. Muller-Reichert, T., Chretien, D., Severin, F. & Hyman, A.A. Structural changes at microtubule ends accompanying GTP hydrolysis: information from a slowly hydrolyzable analogue of GTP, guanylyl (alpha,beta)methylenediphosphonate. *Proceedings of the National Academy of Sciences of the United States of America* **95**, 3661-3666 (1998).
31. Chretien, D., Fuller, S.D. & Karsenti, E. Structure of growing microtubule ends: two-dimensional sheets close into tubes at variable rates. *J Cell Biol* **129**, 1311-1328 (1995).
32. Mandelkow, E.M., Mandelkow, E. & Milligan, R.A. Microtubule dynamics and microtubule caps: a time-resolved cryo-electron microscopy study. *J Cell Biol* **114**, 977-991 (1991).
33. Srayko, M., Kaya, A., Stamford, J. & Hyman, A.A. Identification and characterization of factors required for microtubule growth and nucleation in the early C. elegans embryo. *Dev Cell* **9**, 223-236 (2005).
34. Labbe, J.C., McCarthy, E.K. & Goldstein, B. The forces that position a mitotic spindle asymmetrically are tethered until after the time of spindle assembly. *J Cell Biol* **167**, 245-256 (2004).
35. Mastronarde, D.N., McDonald, K.L., Ding, R. & McIntosh, J.R. Interpolar spindle microtubules in PTK cells. *J Cell Biol* **123**, 1475-1489 (1993).
36. Peterman, E.J. & Scholey, J.M. Mitotic microtubule crosslinkers: insights from mechanistic studies. *Current biology : CB* **19**, R1089-1094 (2009).

37. Magiera, M.M. & Janke, C. Post-translational modifications of tubulin. *Current biology : CB* **24**, R351-354 (2014).
38. Elting, M.W., Hueschen, C.L., Udy, D.B. & Dumont, S. Force on spindle microtubule minus ends moves chromosomes. *J Cell Biol* **206**, 245-256 (2014).
39. Sikirzhytski, V. *et al.* Direct kinetochore-spindle pole connections are not required for chromosome segregation. *J Cell Biol* **206**, 231-243 (2014).
40. Brenner, S. The genetics of Caenorhabditis elegans. *Genetics* **77**, 71-94 (1974).
41. Gusnowski, E.M. & Srayko, M. Visualization of dynein-dependent microtubule gliding at the cell cortex: implications for spindle positioning. *J Cell Biol* **194**, 377-386 (2011).
42. Timmons, L. & Fire, A. Specific interference by ingested dsRNA. *Nature* **395**, 854 (1998).
43. Pelletier, L., O'Toole, E., Schwager, A., Hyman, A.A. & Muller-Reichert, T. Centriole assembly in Caenorhabditis elegans. *Nature* **444**, 619-623 (2006).
44. Muller-Reichert, T., Srayko, M., Hyman, A., O'Toole, E.T. & McDonald, K. Correlative light and electron microscopy of early Caenorhabditis elegans embryos in mitosis. *Methods Cell Biol* **79**, 101-119 (2007).
45. Mastronarde, D.N. Dual-axis tomography: an approach with alignment methods that preserve resolution. *J Struct Biol* **120**, 343-352 (1997).
46. Kremer, J.R., Mastronarde, D.N. & McIntosh, J.R. Computer visualization of three-dimensional image data using IMOD. *J Struct Biol* **116**, 71-76 (1996).
47. Gilbert, P.F. The reconstruction of a three-dimensional structure from projections and its application to electron microscopy. II. Direct methods. *Proc R Soc Lond B Biol Sci* **182**, 89-102 (1972).
48. Stalling, D., Westerhoff, M. & Hege, H.-C. Amira: a highly interactive system for visual data analysis, in *The Visualization Handbook*. (eds. C.D. Hansen & C.R. Johnson) 749–767 (Elsevier, 2005).
49. Weber, B. *et al.* Automated tracing of microtubules in electron tomograms of plastic embedded samples of *C. elegans* embryos. *J Struct Biol* **178**, 129-138 (2012).
50. Redemann, S. *et al.* The segmentation of microtubules in electron tomograms using Amira. *Methods Mol Biol* **1136**, 261-278 (2014).
51. Weber, B. *et al.* Automated stitching of microtubule centerlines across serial electron tomograms. *PloS one* **9**, e113222 (2014).
52. Sbalzarini, I.F. & Koumoutsakos, P. Feature point tracking and trajectory analysis for video imaging in cell biology. *J Struct Biol* **151**, 182-195 (2005).

Acknowledgments

We thank F. Jülicher, D. Needleman, and Dr. Sándalo Roldán-Vargas for continuous discussions and A. Hyman for the feeding clone for *zyg-1* (F59E12.2). The authors are also grateful to Martin Merkel for microtubule segmentation and the electron microscopy facility at MPI-CBG (Dresden) for technical assistance. The Müller-Reichert lab received funding from the Human Frontier Science Program (RGP 0034/2010), the German Research Foundation (DFG grant MU 1423/8-1) and from the Saxonian State Ministry for Science and the Arts (SMWK). J. Baumgart received funding from the European Comission´s 7th Framework Programme grant Systems Biology of Mitosis (FP7_HEALTH-2009-241548/MitoSys). The Brugués lab acknowledges funding from the Human Frontier Science Program (CDA 74/2014) and S. Prohaska was funded by the German Research Foundation (DFG grant PR 1226/4-1) and the FEI Visualization Sciences Group. The Shelley lab acknowledges support from the (USA) National Institutes of Health (1R01GM104976-01) and the Human Frontiers Science Program for support of S. Fürthauer.

Author contributions

This work represents a truly collaborative effort. Each author has contributed significantly to the findings and regular group discussions guided the development of the ideas presented here.

Figure legends

Figure 1. Visualization of spindle and kinetochore microtubules by 3D reconstruction

a, Model of microtubules and chromosomes of a full metaphase spindle. **b**, Model of a half spindle in metaphase. **c-d**, Models of half spindles in anaphase. **e-h**, Corresponding 3D models of KMTs in metaphase and anaphase of the reconstructions as shown in **a-d**. A unique colour is assigned to each spindle and used throughout the publication. The number of microtubules for each reconstruction is indicated. Scale bar 10 μm.

Figure 2. Analysis of kinetochore microtubule attachment sites on chromosomes

a, End-on view of a metaphase plate (metaphase 1A and 1B). Microtubule attachment to individual chromosomes from each pole is indicated by grey dots. As an example, the green line indicates a centre-to-centre distance between two attachment sites. The numbers of microtubules attaching from the visible pole per chromosome are indicated, the numbers for the opposite poles are given in brackets. **b**, Neighbour density analysis of KMT attachment sites. The radial distribution function is normalized by a random seeding with the same density and on the same geometry. **c**, Density (MT/μm^2) of KMTs and SMTs along the half spindle axis from the centrosome to chromosomes. **d**, Ratio of KMTs to SMTs along the half spindle axis from the centrosome to chromosomes aligned at the chromosomes.

Figure 3. Microtubule length distributions

a, Length distribution of AMTs. **b**, Length distribution of SMTs. **c**, Length distribution of KMTs. **d**, Fraction of microtubules within distinct length groups (as indicated by colours) to all microtubules along the spindle axis from centrosomes to chromosomes. **e**, Plot showing the fraction of ends of SMTs located within a region around the centrosome. **f**, Fraction of ends of KMTs located within a region around the centrosome.

Figure 4. Directionality and growth velocity of kinetochore microtubules

a, Schematic image of different regions used for the analysis of EBP-2. **b,** Cross-correlation of EBP-2 comets for $\Delta t = 0.6$ s (blue lines) and smoothed data with a moving average with equal weight (black lines) measured in the areas as indicated in **a**. Velocity and directionality of EBP-2 comets are indicated. **c**, Normalized intensity recovery over time after photobleaching in metaphase. Data is shown in blue, mean (□ s.e.m.) in black. Measured half time recovery is indicated. **d**, Position of the lowest intensity of the bleach mark over time. Values for the different datasets are shown in blue, the mean (□ s.e.m.) is shown in black.

Figure 5. Interaction of spindle and kinetochore microtubules

a, Parameters for the characterization of microtubule-microtubule interactions. *d:*, distance from centrosome centre to a microtubule (green); *a:* closest centre-to-centre distance between two microtubules (green and red); and □*:* opening angle between two

microtubules. **b**, Illustration of the positions of 25 % and 75 % half-spindle length. **c-d**, Neighbourhood density analysis of microtubules at 25 % and 75 % half spindle length for different centre-to-centre distances normalized by the radial distribution function of random points with the same density on the same geometry. **e**, Percentage of KMTs that can potentially connect to the centrosome as a function of interaction parameters *a* and α. *d* is set to 1.2 μm in metaphase. **f**, Number of interactions necessary to link a KMT to the centrosome for a specific set of parameters (here $a = 80$nm, $\alpha = 35°$). '*not'* indicates the number of microtubules that cannot establish a connection, '*0'* represents the microtubules that directly connect to the centrosome.

Figure 6. Models of kinetochore microtubule formation in *C. elegans*

a, Microtubule flux model: SMTs grow out from the centrosome and will either undergo catastrophe or, upon connecting to a kinetochore, become a KMT. KMTs will then transition to a shrinking state, in which they depolymerise from their plus-end. The plus-end of the KMT remains connected to the kinetochore during depolymerisation. **b**, Microtubule depolymerising model, SMTs grow out from the centrosome and will either undergo catastrophe or, upon connecting to a kinetochore, become a KMT. In this model SMTs as well as KMTs can also depolymerise from their minus-end during their lifetime. **c**, Detachment Model, SMTs grow out from the centrosome and will either undergo catastrophe or, upon connecting to a kinetochore become a KMT. KMTs will then transition to a shrinking state, in which they depolymerise from their minus-end.

Extended Data Figure 1. Workflow of large-scale spindle reconstructions by 3D electron tomography

a, 2 x 3 montages (outlined in dark red, individual tomograms composing the montages are outlined in light red) are acquired and joined in X and Y to cover the entire area of the spindle. The size of a single tomogram, the magnification, and pixelsize are indicated. **b**, Approximately 25 consecutive sections have to be acquired to cover the spindle volume. **c**, Microtubules (green) are automatically traced and manually corrected using the AMIRA software. This software is also used to stitch the individual sections in *z*. **d**, Features like chromosomes (purple) or the nuclear envelope (light blue) can be segmented manually.

Extended Data Figure 2. Reconstruction of a central spindle in metaphase

a, Model of a metaphase spindle covering the volume around the chromosomes. **b**, KMTs of the dataset as shown in **a**. The number of KMTs is indicated in the bottom left corner. Scale bar, 10 μm.

Extended Data Figure 3. KMT attachment correlates with chromosome area

a, Correlation of chromosome surface area and number of attached KMTs for two metaphase datasets Scale bar, 1 μm. **b**, Average density of KMT attachment sites on chromosomes in metaphase and anaphase.

Extended Data Figure 4. Microtubules in early prometaphase and monopolar spindles

a, Model of chromosomes (magenta), nuclear envelope (grey) and microtubules (green) in a one-cell *C. elegans* embryo at early prometaphase. **b**, Two-cell *C. elegans* embryo after *zyg-1* (RNAi) labeled with β-tubulin::GFP and Histone::GFP. **c**, Model of SMTs in three consecutive tomographic sections of a monopolar spindle as shown in **b**. **d**, Model of the KMTs as identified in **c**. Scale bar, 10 μm.

Extended Data Figure 5. Analysis of microtubule end conformation

a, Percentage of open (empty bars) and closed KMT ends (filled bars) at the centrosomes and kinetochores in metaphase (black outline) and anaphase (grey outline). **b**, Percentage of end-conformations of both KMT ends in metaphase (black bars) and anaphase (grey bars). **c,** Plot of the fraction of open and closed AMT ends with respect to the distance from the centrosome for metaphase 1A (blue), anaphase 1 (red) and anaphase 2 (yellow). Open circles represent open ends, filled circles closed ends. **d,** Plot of the fraction of open and closed SMT ends with respect to the distance from the centrosome.

Extended Data Figure 6. Results from the stochastic microtubule flux model:

a, KMT length distribution. **b,** SMT length distribution. **c**, SMT minus end distribution. For **a**, **b**, **c** we display the long expectation value of the model (solid black line) plus one (dark grey shaded region) and two (light grey shaded region) standard deviations. The

coloured circles show measured data. **d**, time-course of the total microtubule number (green) and KMT number (red) for a typical instance of the simulation with a depolymerisation velocity of $v_d = 0.02\ \mu m/s$

Extended Data Figure 7. Results from the stochastic microtubule depolymerisation model:

a, KMT length distribution. **b,** SMT length distribution. **c**, SMT minus end distribution. For **a**, **b**, **c** we display the long expectation value of the model (solid black line) plus one (dark grey shaded region) and two (light grey shaded region) standard deviations. The coloured circles show measured data. **d**, time-course of the total microtubule number (green) and KMT number (red) for a typical instance of the simulation with a depolymerisation velocity of $v_d = 0.05\ \mu m/s$ and a switching rate from growth to shrinkage of $r = 0.1$ Hz.

Extended Data Figure 8. Results from the stochastic microtubule detachment model:

a, KMT length distribution. **b,** SMT length distribution. **c**, SMT minus end distribution. For **a**, **b**, **c** we display the long expectation value of the model (solid black line) plus one (dark grey shaded region) and two (light grey shaded region) standard deviations. The coloured circles show measured data. **d**, time-course of the total microtubule number (green) and KMT number (red) for a typical instance of the simulation with a

depolymerisation velocity of $v_d = 0.17\ \mu m/s$ and a switching rate from growth to shrinkage of r = 0.5 Hz, which is twice the rate of catastrophe.

Extended Data Figure 9. Z-stack histograms of microtubule endpoints

a,c,e,g, Histograms of the number of microtubule endpoints within each section and at the boundary of each section as an estimate of the stitching quality of the individual datasets. Only endpoints in the intersection of all slices are analysed. **b,d,f,h**, Average of the tomogram area over all slices for each individual data set as shown in **a**,**c**,**e**,**g**.

Table 1. Parameters for the three stochastic models.

The adjustable parameters were set in bold italic. All other values are estimated from experimental observations.

Supplementary movie 1, **Illustrative visualization of the reconstruction of a complete metaphase spindle dataset in *C. elegans***

The kinetochore microtubules are depicted in red, astral and spindle microtubules in green. A segmentation of the chromosomes is shown as blue surface.

Supplementary movie 2, **Illustrative visualization of the reconstruction of a complete metaphase spindle dataset in *C. elegans***

Here we show a rotation around the chromosomes.

Supplementary movie 3, **Illustrative visualization of the reconstruction of a complete metaphase spindle dataset in *C. elegans***

Here we show a close up of the kinetochore microtubules.

Supplementary movie 4, **EBP-2::GFP in the C. elegans metaphase**

Motion of EBP-2::GFP comets in metaphase in *C.elegans*. Exposure 150 ms, frame rate 200 ms.

Supplementary movie 5, **Fluorescence recovery after photobleaching (FRAP) in a *C. elegans* metaphase**

FRAP in a Histone::GFP and b-tubulin::GFP tagged *C. elegans* embryo in metaphase. Exposure 100 ms, frame rate 500 ms.

Supplementary movie 6, **Laser microsurgery in a *C. elegans* metaphase**

Laser microsurgery in in a β-tubulin::GFP tagged *C. elegans* embryo. Exposure 300 ms, frame rate 5 s.

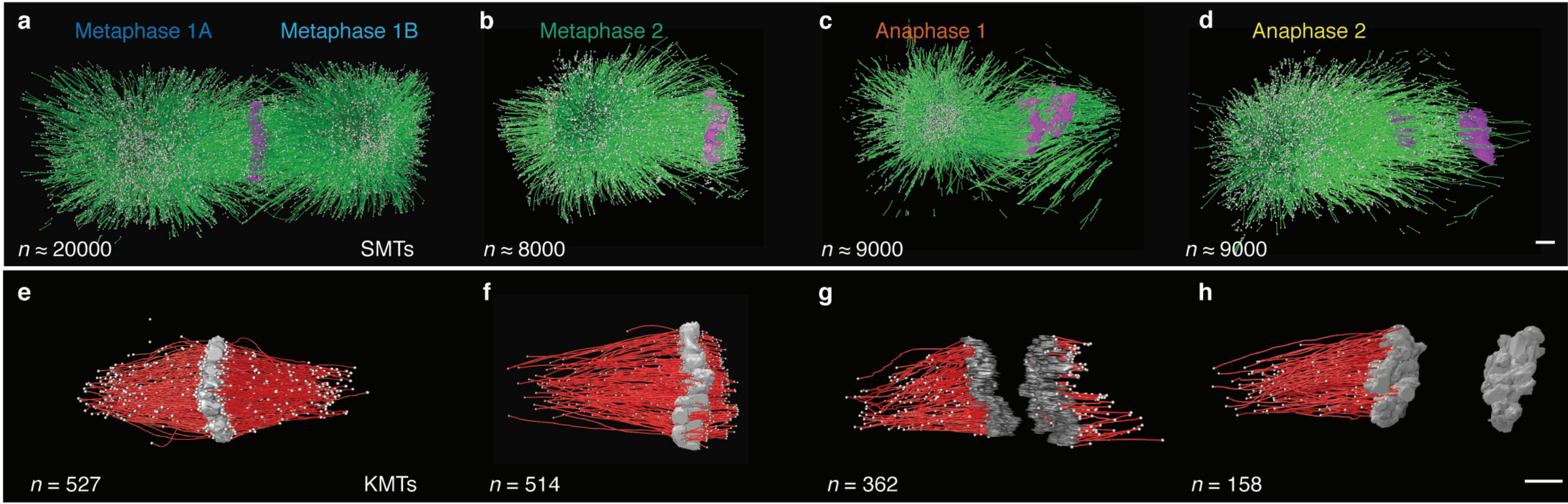
a
Metaphase 1A
Metaphase 1B
n ≈ 20000
SMTs
b
Metaphase 2
n ≈ 8000
c
Anaphase 1
n ≈ 9000
d
Anaphase 2
n ≈ 9000
e
n = 527
KMTs
f
n = 514
g
n = 362
h
n = 158

Figure 1

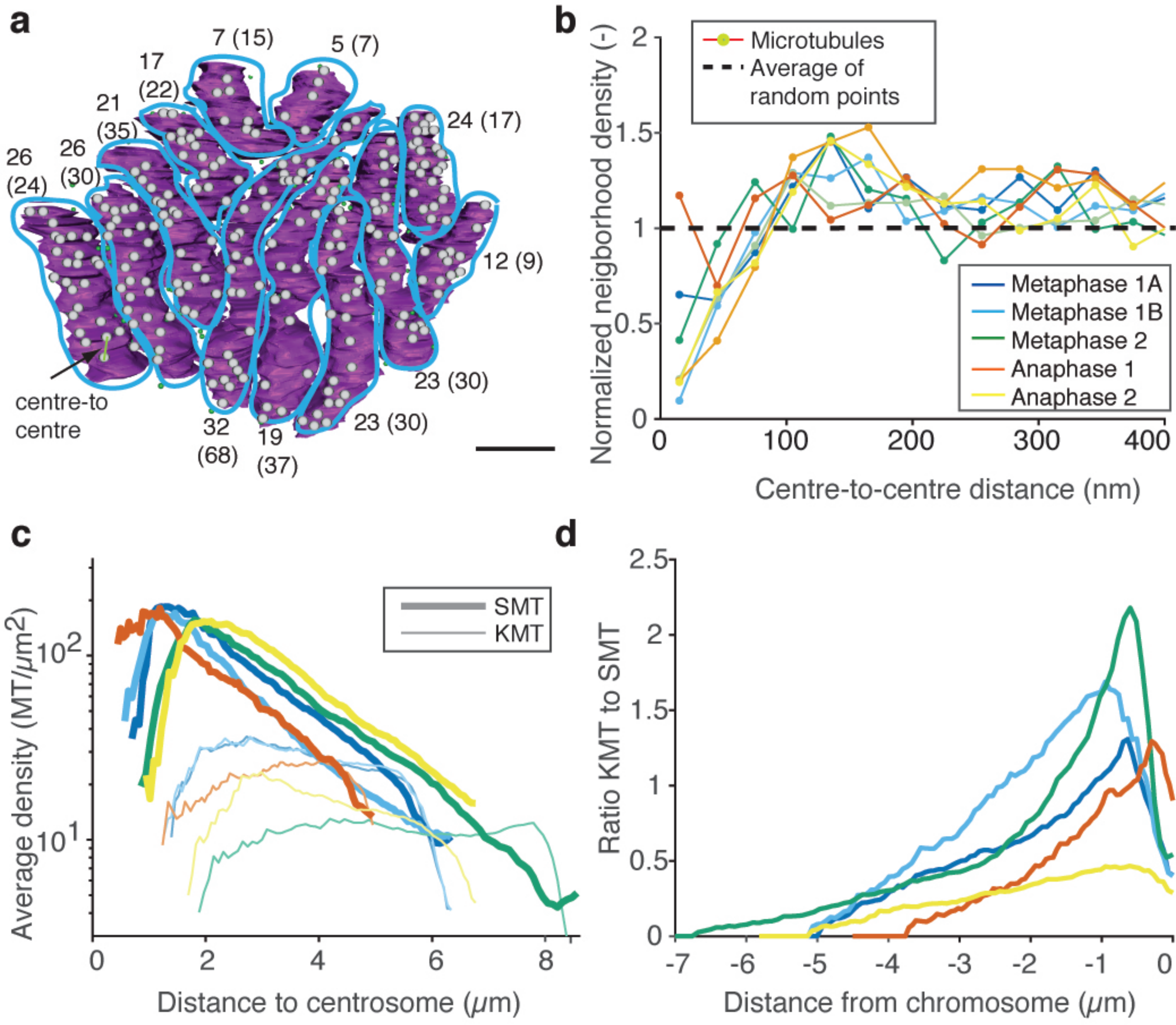
a
7 (15)
5 (7)
17
(22)
21
(35)
26
(30)
26
(24)
24 (17)
12 (9)
23 (30)
23 (30)
19
(37)
32
(68)
centre-to
centre
b
Microtubules
Average of
random points
Metaphase 1A
Metaphase 1B
Metaphase 2
Anaphase 1
Anaphase 2
Normalized neigborhood density (-)
Centre-to-centre distance (nm)
c
SMT
KMT
Average density (MT/μm²)
Distance to centrosome (μm)
d
Ratio KMT to SMT
Distance from chromosome (μm)

Figure 2

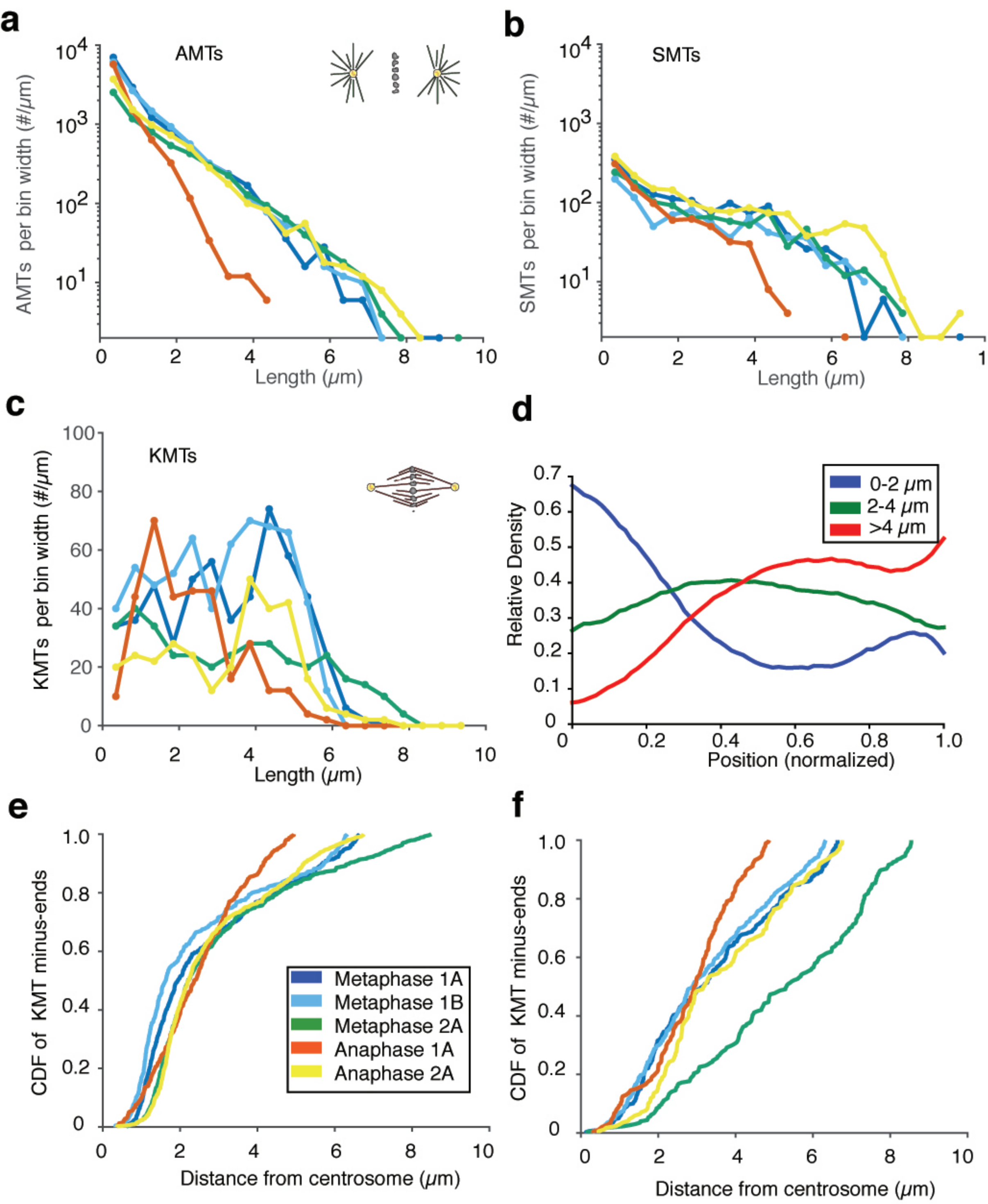
a
AMTs
AMTs per bin width (#/μm)
Length (μm)
b
SMTs
SMTs per bin width (#/μm)
Length (μm)
c
KMTs
KMTs per bin width (#/μm)
Length (μm)
d
0-2 μm
2-4 μm
>4 μm
Relative Density
Position (normalized)
e
Metaphase 1A
Metaphase 1B
Metaphase 2A
Anaphase 1A
Anaphase 2A
CDF of KMT minus-ends
Distance from centrosome (μm)
f
CDF of KMT minus-ends
Distance from centrosome (μm)

Figure 3

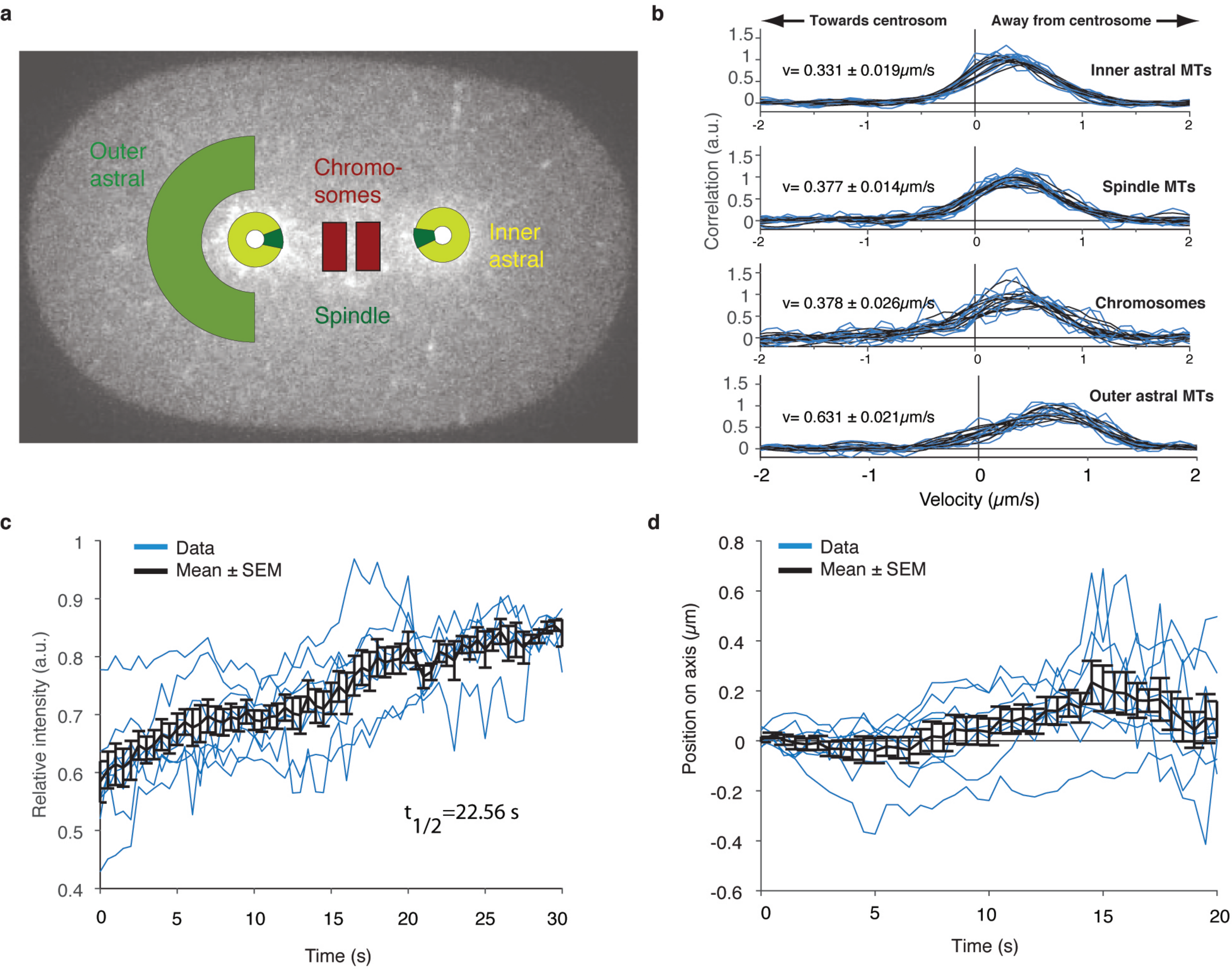
a
Outer astral
Chromo-somes
Inner astral
Spindle
b
Towards centrosom
Away from centrosome
Correlation (a.u.)
v= 0.331 ± 0.019μm/s
Inner astral MTs
v= 0.377 ± 0.014μm/s
Spindle MTs
v= 0.378 ± 0.026μm/s
Chromosomes
v= 0.631 ± 0.021μm/s
Outer astral MTs
Velocity (μm/s)
c
Data
Mean ± SEM
Relative intensity (a.u.)
t1/2=22.56 s
Time (s)
d
Data
Mean ± SEM
Position on axis (μm)
Time (s)

Figure 4

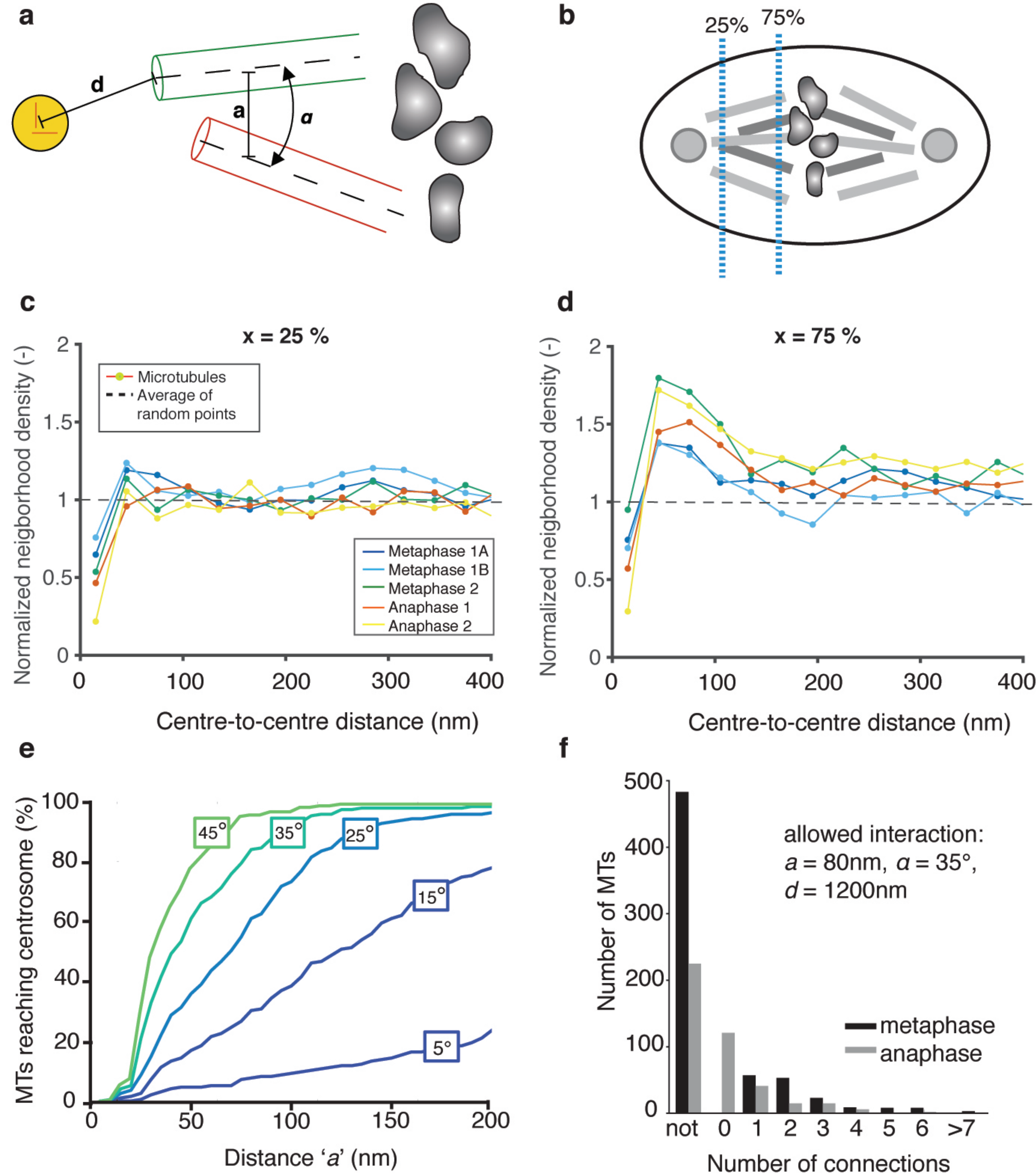
a
d
a
α
b
25%
75%
c
x = 25 %
Normalized neigborhood density (-)
Microtubules
Average of random points
Metaphase 1A
Metaphase 1B
Metaphase 2
Anaphase 1
Anaphase 2
Centre-to-centre distance (nm)
d
x = 75 %
Normalized neigborhood density (-)
Centre-to-centre distance (nm)
e
MTs reaching centrosome (%)
45°
35°
25°
15°
5°
Distance 'a' (nm)
f
Number of MTs
allowed interaction:
a = 80nm, α = 35°,
d = 1200nm
metaphase
anaphase
not
Number of connections

Figure 5

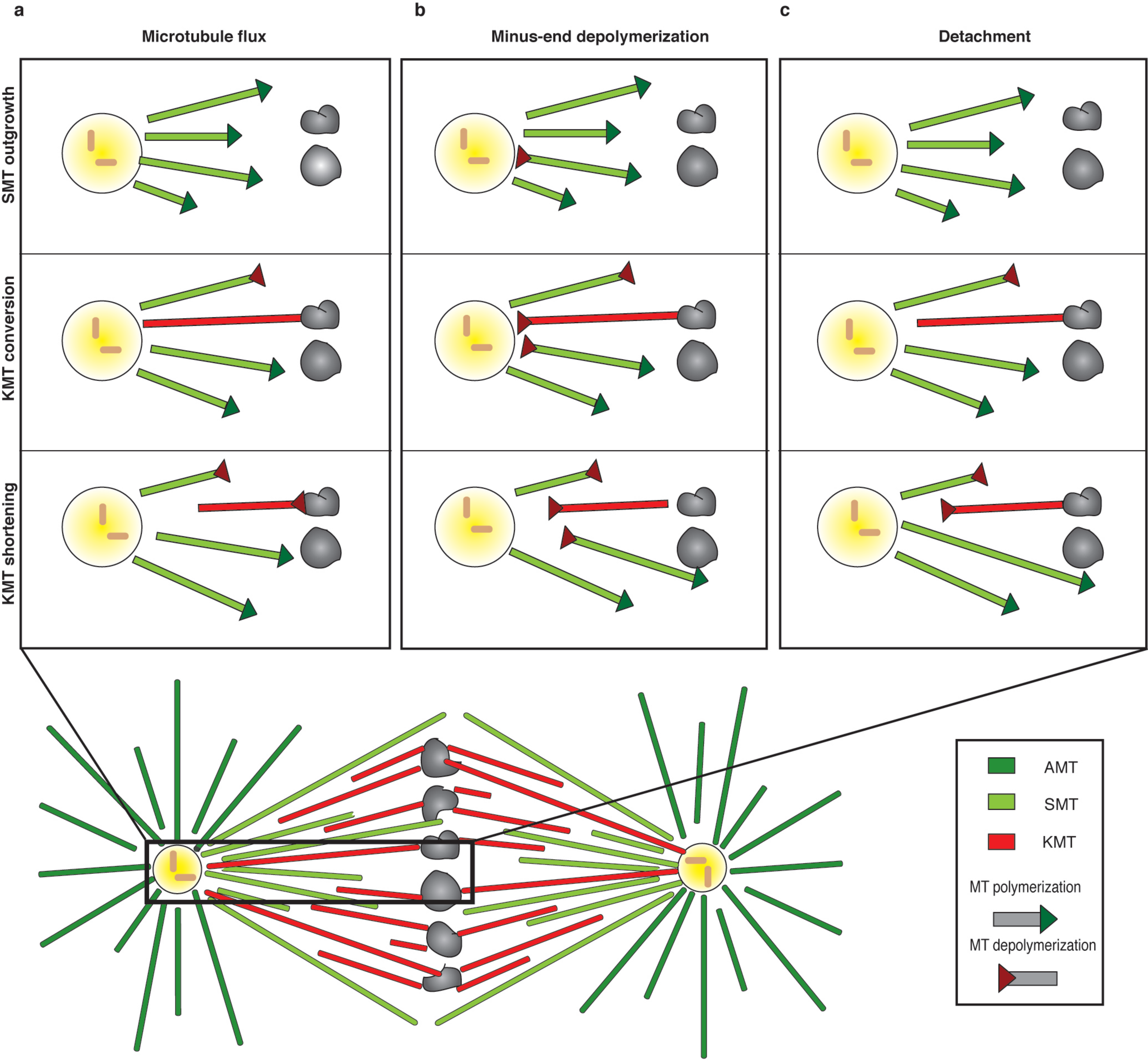
a
b
c
Microtubule flux
Minus-end depolymerization
Detachment
SMT outgrowth
KMT conversion
KMT shortening
AMT
SMT
KMT
MT polymerization
MT depolymerization

Figure 6

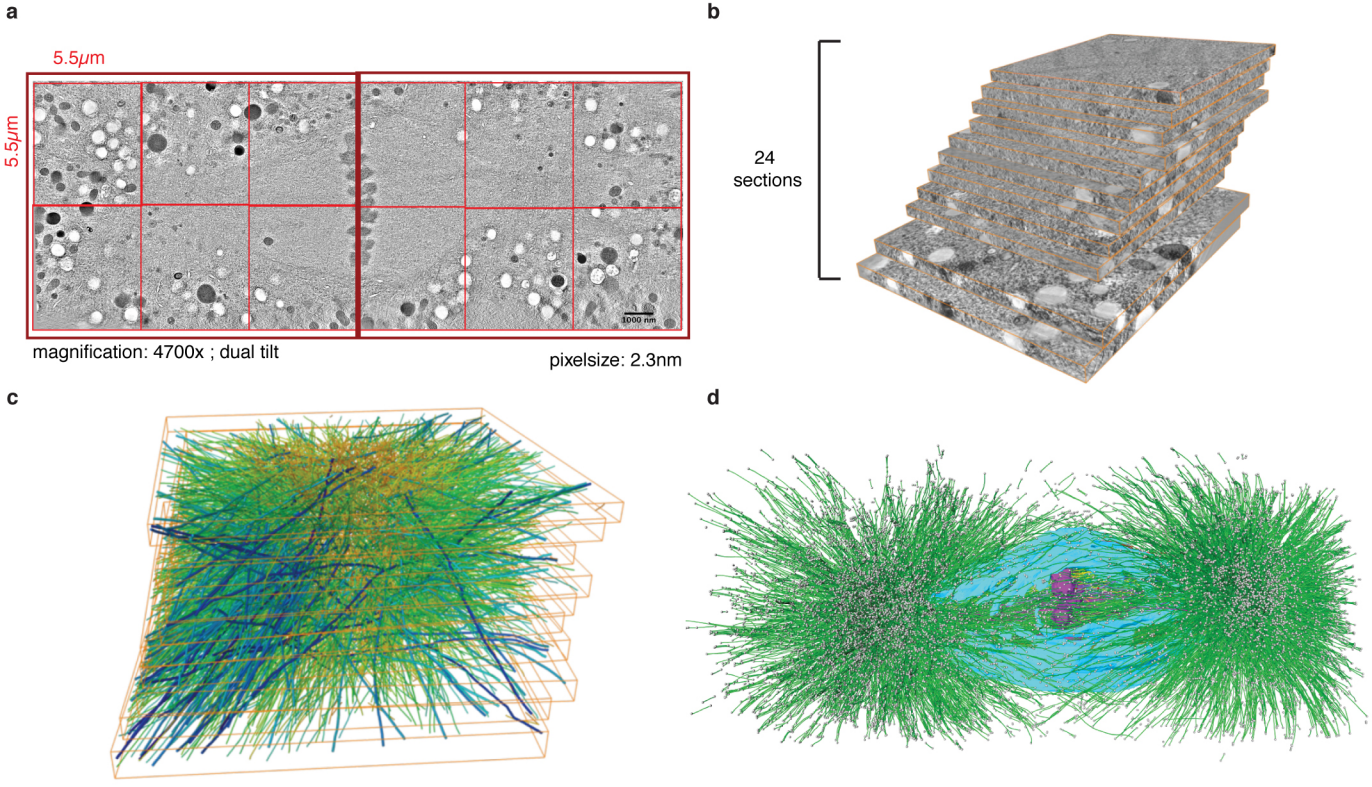

Extended Data Figure 1

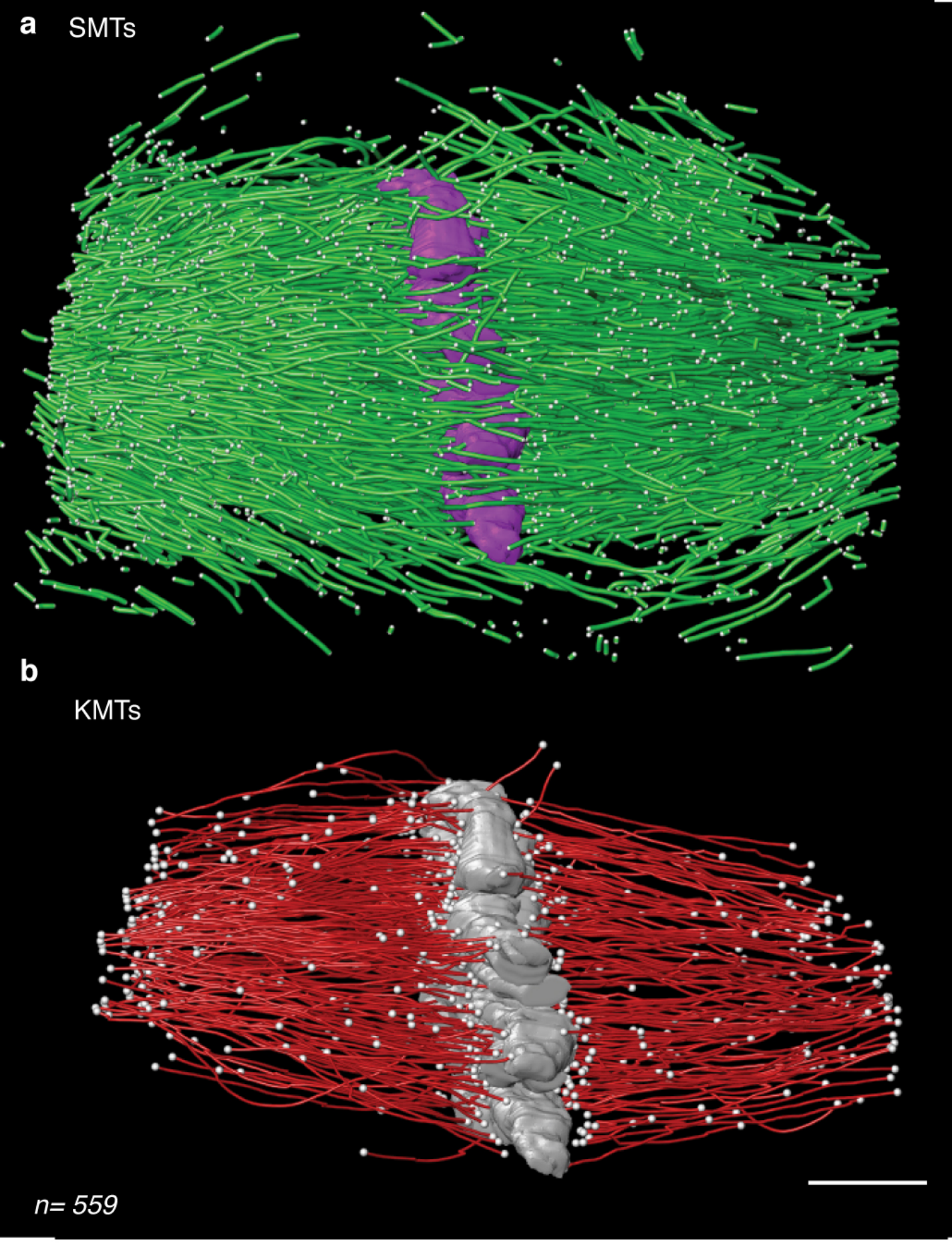

Extended Data Figure 2

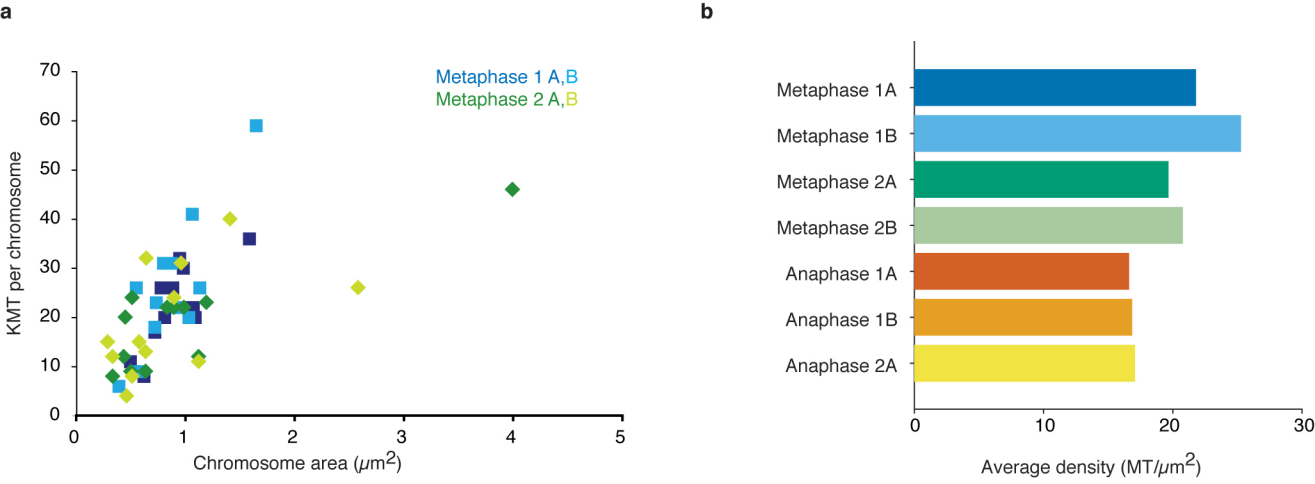

Extended Data Figure 3

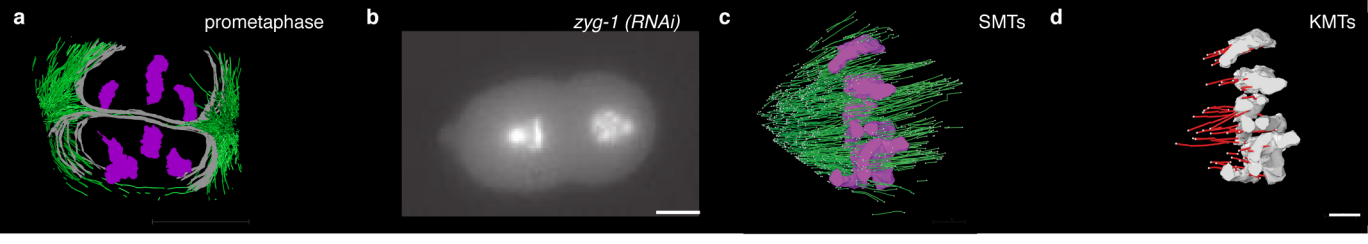

Extended Data Figure 4

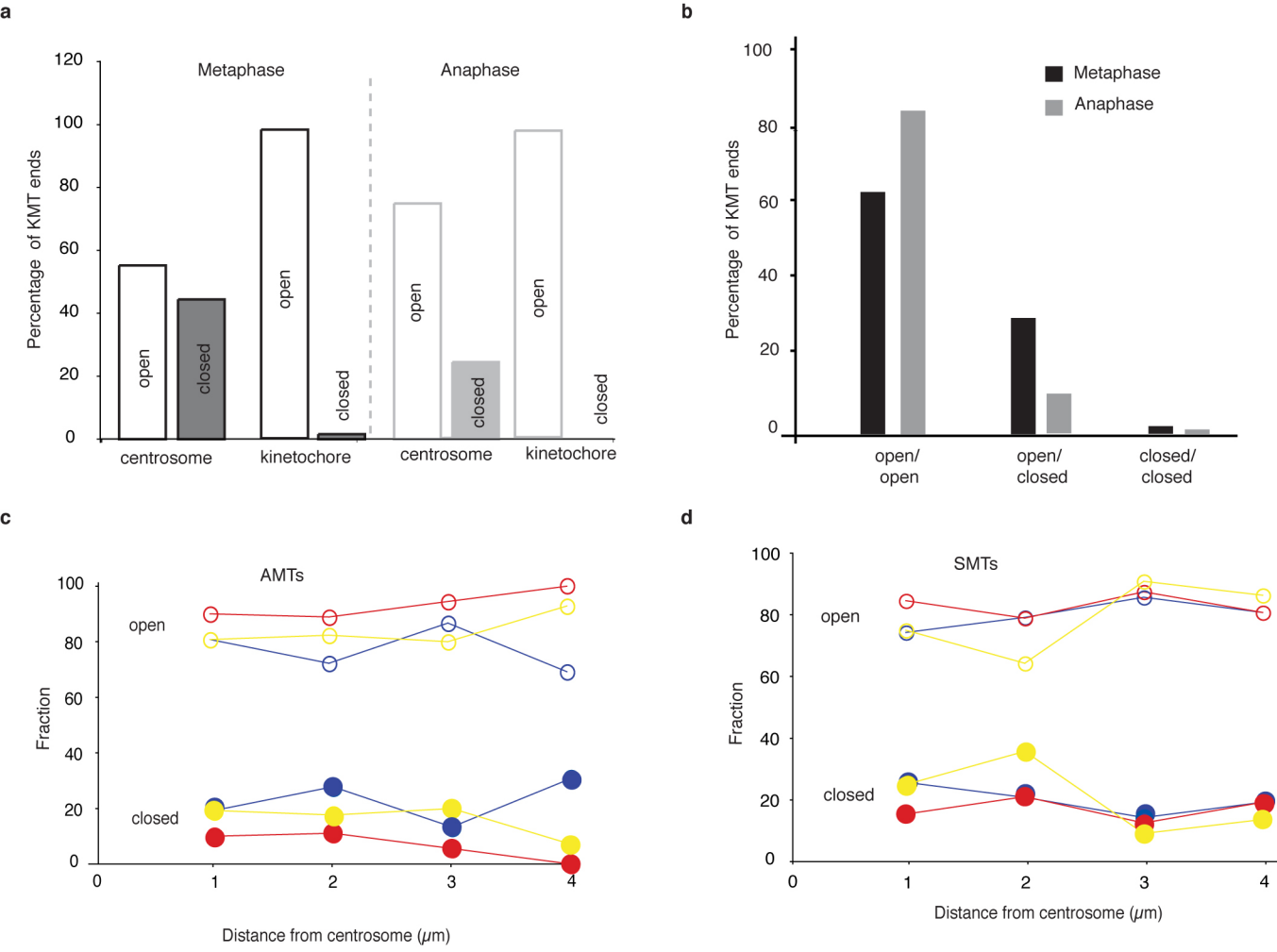

Extended Data Figure 5

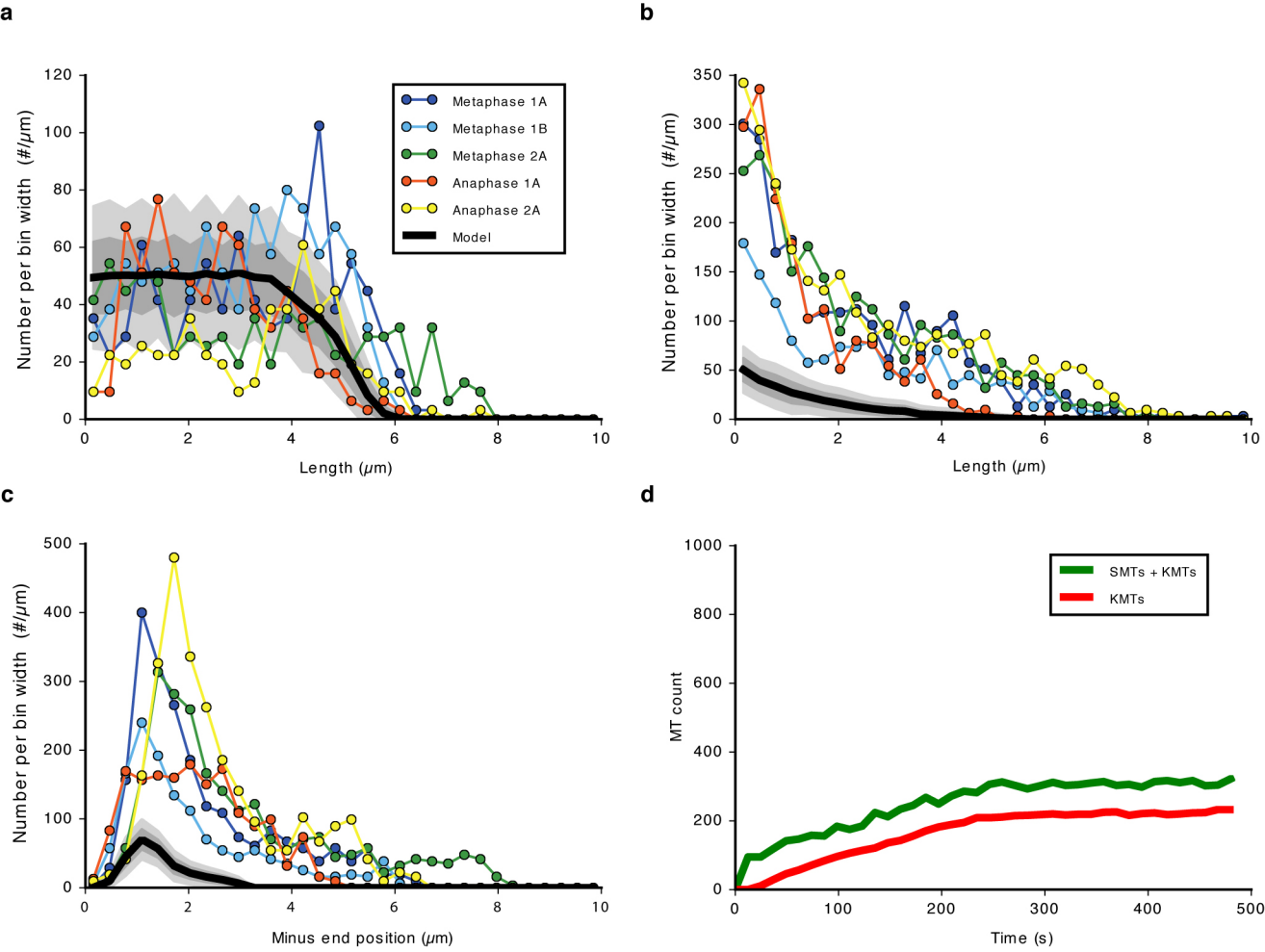

Extended Data Figure 6

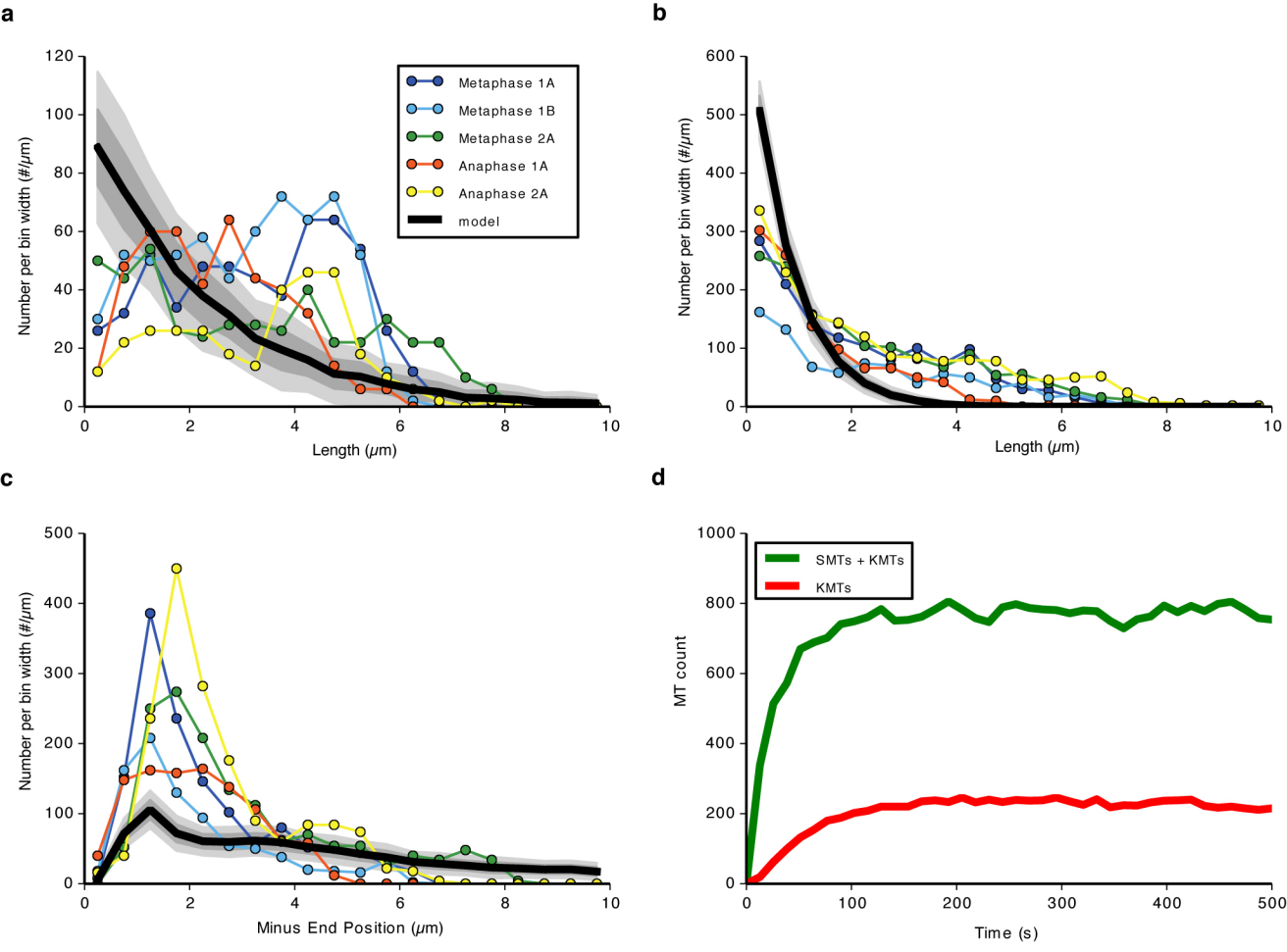

Extended Data Figure 7

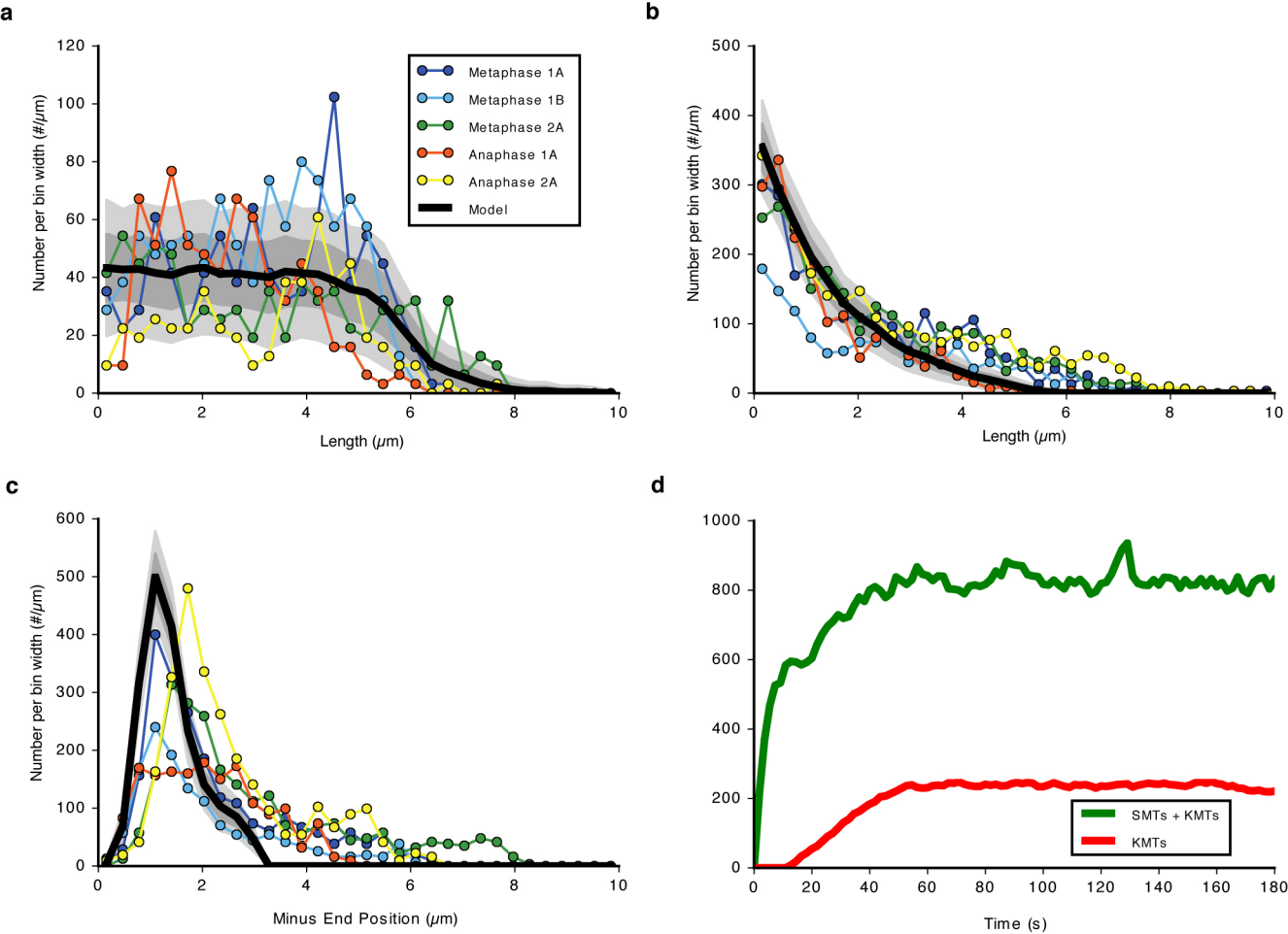

Extended Data Figure 8

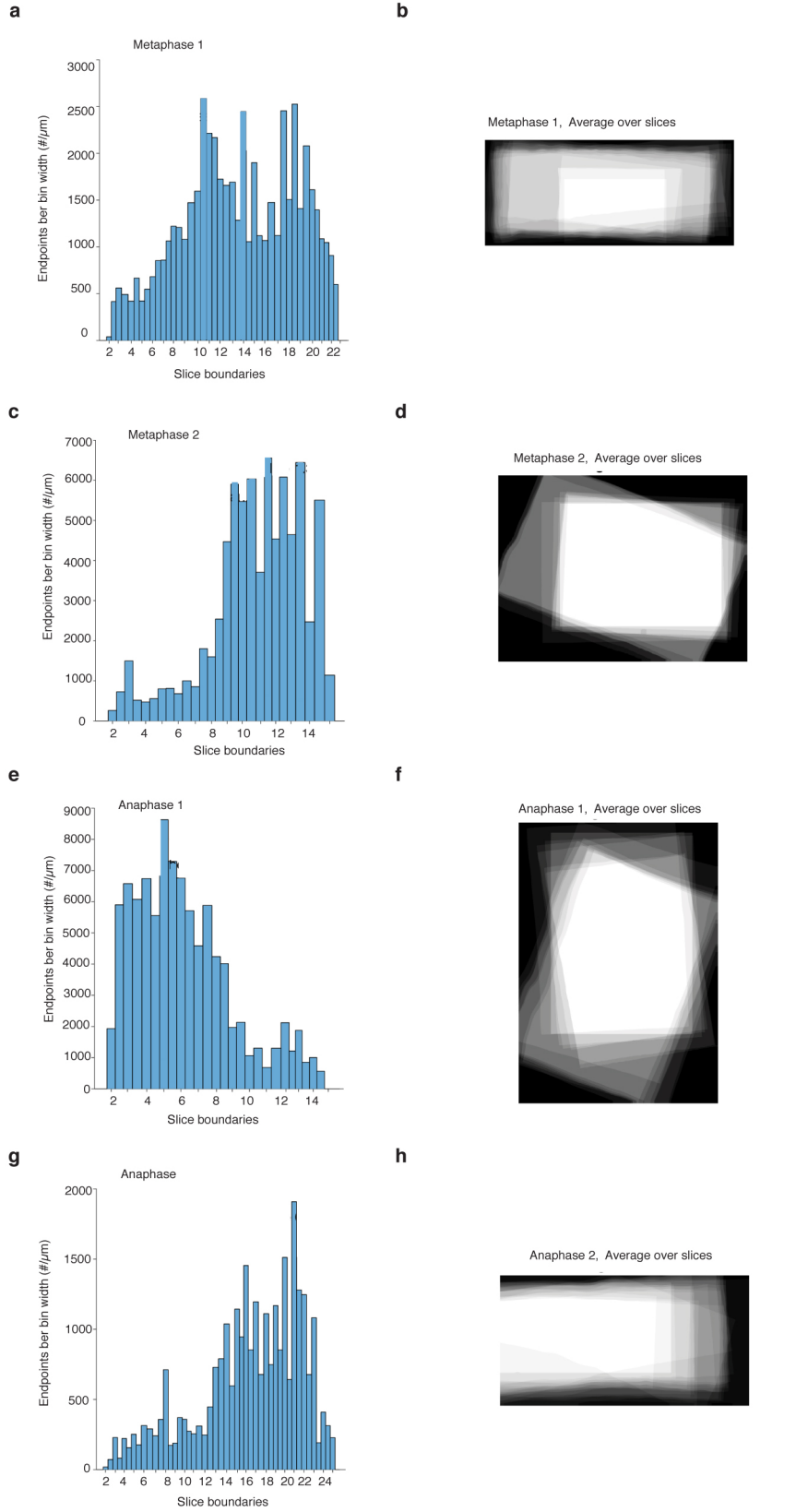

Extended Data Figure 9

	Flux Model	**Depolymerization Model**	**Detachment Model**
Growth Velocity v_g	0.4 μm/second	0.4 μm/second	0.4 μm/second
Depolymerization Velocity v_d	0.02 μm/second	***0.05 μm/second***	***0.17 μm/second***
Centrosome-Chromosome Distance *L*	6.5 μm	6.5 μm	6.5 μm
Catastrophe rate	0.25 Hz	0.25 Hz	0.25 Hz
Switching rate *r* for KMTs	Instantaneous	***0.1 Hz***	0.5 Hz
Switching rate *r* for SMTs	0	***0.1 Hz***	0